International Journal of Heat and Mass Transfer 112 (2017) 300–317

Contents lists available at ScienceDirect

International Journal of Heat and Mass Transfer

journal homepage: www.elsevier.com/locate/ijhmt

Melt dynamics and melt-through time in continuous wave laser heating of metal films: Contributions of the recoil vapor pressure and Marangoni effects

Alexey N. Volkov [a,*], Leonid V. Zhigilei [b]

[a] University of Alabama, Department of Mechanical Engineering, Tuscaloosa, AL 35407, USA
[b] University of Virginia, Department of Materials Science and Engineering, Charlottesville, VA 22904, USA

ARTICLE INFO

Article history:
Received 21 February 2017
Received in revised form 16 April 2017
Accepted 17 April 2017

Keywords:
CW laser melting
Hydrodynamic modelling
Recoil effect
Marangoni effect
Melt-through time

ABSTRACT

The relative contributions of evaporation and melt expulsion due to the recoil vapor pressure and Marangoni effects to the laser damage and melt dynamics in continuous wave (CW) laser interactions with free-standing aluminum films are evaluated in two-phase hydrodynamic simulations. In order the establish the dominant damage mechanisms in different irradiation regimes, the results of hydrodynamic simulations are compared with the predictions of several simplified models that only account for a subset of the involved processes. The hydrodynamic simulations performed in the range of film thickness from 0.2 mm to 4 mm and laser spot radius from 0.1 mm to 1 cm reveal only a marginal effect of the Marangoni stresses on the overall picture of melt flow and the melt-through time. The recoil pressure effect, on the contrary, is capable of strongly decreasing the melt-through time in a certain range of laser intensity. At laser intensities below this range the melting process is largely defined by heat transfer in the radial direction, while at laser intensities above this range the thickness of the molten pool and the efficiency of melt expulsion decrease and evaporation becomes the primary mechanism of material removal from the center of the laser spot. The range of laser intensities where the melt-through time is controlled by the recoil pressure effect is not unique and depends on the film thickness. A simple two-phase one-dimensional thermal model of laser melting, where melt expulsion due to the recoil pressure effect is accounted for based on the Bernoulli integral, is developed and found to be capable of accurate prediction of the melt-through time above a certain level of laser intensity. The one-dimensional thermal model captures all qualitative trends revealed in the direct hydrodynamic simulations and can be used as a robust engineering tool for the first-order estimation of the conditions for CW laser damage of metal films.

1. Introduction

High-power continuous wave (CW) lasers are used in various industrial applications that involve welding, drilling, and cutting of various materials [1], as well as in studies aimed at evaluation of laser damage in a beamed energy attack [2,3]. The irradiation conditions in CW laser – material interactions are characterized by broad ranges of laser spot diameters, from tens of micrometers [4] to tens of centimeters [2,5], and laser intensities, up to 10^9 W cm^{-2}, which are accessible with either powerful CO_2 lasers or compact CW laser systems based, e.g., on single-mode fiber lasers [4,6]. Even the maximum levels of power density accessible with CW lasers are still orders of magnitude smaller than the energy densities that can be generated with short and ultra-short pulsed lasers [7]. Correspondingly, the extreme levels of superheating required for the onset of volumetric ablation through phase explosion or explosive boiling, which play a major role in material removal with short pulsed lasers [8–10], are not achieved with CW lasers.

The primary mechanisms of CW laser damage and material removal are evaporation and melt expulsion from the center of the laser spot. The latter process of radial outflow of the melt from the center of the laser spot usually results in the formation of a large rim of resolidified material around the spot edge [1,7] or spattering of a liquid layer [4]. The traces of the melt flow are usually clearly visible at experimental images of metal surfaces irradiated by high-power CW lasers [6]. The melt expulsion decreases the characteristic thickness of the molten pool in the central part

* Corresponding author.
E-mail address: avolkov1@ua.edu (A.N. Volkov).

http://dx.doi.org/10.1016/j.ijheatmasstransfer.2017.04.100
0017-9310/

of the laser spot and increases the velocity of propagation of the solid-liquid interface, thus, rising the efficiency of laser drilling and reducing the melt-through time in laser damage to metal films. An additional process that may strongly affect the rate of material removal and the characteristics of laser damage is the heterogeneous oxidation at the laser spot. The oxidation can lead to the formation of an oxide film that can substantially change the optical, thermal, and mechanical properties of the surface. The energy release during the exothermal heterogeneous oxidation and gas-phase burning of the vaporized material can serve as a source of secondary heating of the irradiated surface [11] and increase the rate of material removal from the center of the laser spot [12].

The two main driving forces responsible for melt expulsion from the laser spot are the recoil pressure created by the active evaporation process and the Marangoni effect. Both of these effects arise from nonhomogeneous, often Gaussian [7], distribution of the deposited energy across the laser spot and, correspondingly, nonhomogeneous distribution of surface temperature.

The melt expulsion by the recoil pressure is caused by the spatial variation of the normal stress exerted by vapor pressure within the laser spot. The gradient of vapor pressure induces melt flow from the high-pressure region at the spot center towards the low-pressure periphery of the molten pool [13–15]. A substantial influence of the recoil vapor pressure on the dynamics of the molten pool was also observed in recent particle-resolved multiphase simulations of Selective Laser Melting (SLM) of metal powders, e.g., [16], where the recoil pressure was found to play an essential role in trapping small voids inside resolidified material in a process that involves collapse of depressions appearing at the surface of the molten pool in the regime of keyhole formation.

The Marangoni or thermocapillary effect involves the formation of strong tangential stresses on a non-uniformly heated surface of the molten pool due to the dependence of the surface tension on temperature, e.g., [17]. Since the surface tension of liquid metals decreases with increasing temperature, e.g., [18], the Marangoni stresses act in the direction opposed to the direction of the surface temperature gradient. In the case of laser heating, the temperature usually peaks at the center of the laser spot and the Marangoni stresses induce melt flow from the center to the periphery of the spot, thus providing an additional contribution to melt expulsion. At high heating rates and small thicknesses of the molten layer, the Marangoni stresses can lead to the rupture of the molten layer [19], melt spattering, and formation of droplets [20].

At very high laser intensities, the melt expulsion can result in the removal of most of the melt [4] from the irradiated area. At moderate laser intensities, however, the efficiency of both mechanisms of the melt expulsion discussed above decreases, and an external gas flow applied either as a shear flow parallel to the irradiated target [3,5,21] or a jet directed towards the center of the spot [22,23] is used to intensify the melt removal and increase the speed of laser processing or cutting. The combination of material softening at temperatures close but not exceeding the melting temperature and an airflow-induced pressure difference between two surfaces of the irradiated film can also contribute to the damage of a metal film heated by a CW laser before the film melts to its full depth, as has been discussed in Ref. [2]. In the absence of an external gas flow or a substantial pressure difference on the two sides of the film (e.g., in irradiation of a pressurized container), one can expect that the laser damage is largely defined by the melting of the film to its full depth.

The majority of computational studies that apply hydrodynamic modeling to the analysis of laser melting are focused on large aspect ratio (ratio of the depth of the laser keyhole to its diameter) laser drilling at high laser intensities, when material removal from the keyhole is dominated by vaporization and melt expulsion caused by the recoil effect, e.g. [24]. The relative importance of the individual mechanisms responsible for the melt expulsion and removal is typically not discussed, although, for very high laser intensities characteristic for ultrashort laser pulses, a negligible contribution of the Marangoni effect has been reported for laser melting of glass targets [25]. For moderate laser intensities and moderate-to-small keyhole aspect ratios, the reports of pure hydrodynamic simulations are scarce (see, e.g., review in Ref. [1]) and the relative contributions of the recoil and Marangoni effects to the melt removal and target damage are not well understood. The estimations made by Semak and Matsunawa [13] predicted the overall strong effect of the recoil pressure, which was confirmed in simulations performed by Yilbas and Mansoor [14]. At the same time, Ajaev and Willis [19] and Willis and Xu [20] reported a negligible effect of the recoil pressure on the melt flow in laser melting of thin films, which was dominated by thermocapillary stresses in their simulations. Han and Liou [26] also concluded that the melt flow is mainly caused by the thermocapillary stresses, but pointed out that the contribution of the recoil pressure is not small and should not be neglected.

The goal of the computational study reported in the present paper is to explore the contributions of the vapor recoil and Marangoni effects to the CW laser melting and damage of aluminum films in a broad range of process parameters realized in both laser damage and material processing applications. The processes of laser heating, melting, and melt flow are investigated in a series of simulations performed with a two-phase hydrodynamic model. The films with thicknesses that do not exceed the laser spot diameter are considered, and the simulations are continued until the time when the melting front reaches the back surface of the film. This time is further referred to as the melt-through time and is considered as the primary measure of the laser damage. One of the main finding of the simulations is that the Marangoni effect only marginally changes the melt-through time for all conditions considered in this study. This conclusion contradicts the results previously reported in Refs. [19,20,26]. At the same time, for a fixed film thickness, there is a certain range of laser intensities, where the recoil vapor pressure has a strong effect on the melting process and reduces the melt-through time by a factor of two as compared to the simulations where melt expulsion is not taken into account. We also show that the results of two-dimensional (2D) hydrodynamic simulations are in qualitative (and, for sufficiently high laser intensities, quantitative) agreement with results obtained with a simple and robust one-dimensional (1D) thermal model, where the effect of melt expulsion is accounted for based on the Bernoulli integral.

2. Hydrodynamic model of CW laser melting

The hydrodynamic simulations are performed for a planar free-standing aluminum film of thickness H_0 irradiated by a CW laser. The laser is assumed to irradiate the target in the direction normal to the initial film surface, producing an axially symmetric Gaussian distribution of laser intensity with respect to the center of the laser spot, as schematically shown in Fig. 1(a). Absorption of laser energy by the target material induces its melting and flow of the molten material. These processes are assumed to be 2D and axisymmetric and are considered in the central part of the computational domain shown as $OA'B'C$ in Fig. 1(b). In the periphery of the computational domain, beyond the region affected by laser melting, the heat conduction equation is solved to ensure realistic representation of heat transfer from the central part of the laser spot. The position of the free surface BC is described by the height function $H_w(r,t)$, where r is the radial distance from the axis of

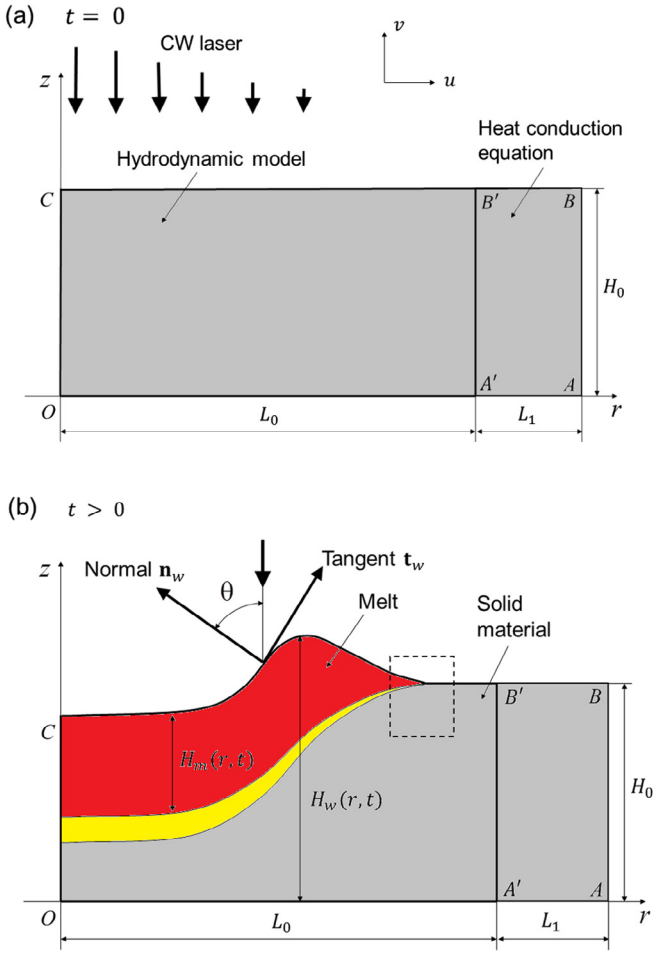

Fig. 1. Sketch of the computational domain used in hydrodynamic simulations of CW laser melting of a free-standing aluminum film at the initial time $t = 0$ (a) and in the course of melting (b). The computational domain is outlined by the thermally insulated bottom surface of the film OA, lateral boundary AB maintained at a constant temperature T_0, top surface BC, and the axis of symmetry OC. The hydrodynamic model is used in the central part of the computational domain, $OA'B'C$, with the lateral size L_0 chosen to ensure that the whole molten pool is located within this part of the system. In the outer part of the computational domain, $A'ABB'$, the heat conduction equation is solved and the lateral size L_1 is chosen to ensure that the temperature field in the inner domain $OA'B'C$ is not affected by the constant-temperature boundary condition applied at the boundary AB. The two parts of the computational domain are not shown to scale, as the size L_1 is chosen to be equal to or larger than L_0. In the numerical model, the sharp melting front is replaced by the two-phase zone (yellow) dividing the solid (gray) and liquid (red) material. Simulations are performed until the melting front reaches the bottom surface of the film, so that the deformation of the bottom surface is not taken into account. The dashed rectangle in (b) outlines the region for which computational mesh is shown in Fig. 2. (For interpretation of the references to color in this figure legend, the reader is referred to the web version of this article.)

symmetry OC and t is time. In the model of melting, the density changes at the solid-liquid interface are neglected and both meting and melt flow are described by the two-phase hydrodynamic model based on the full Navier-Stokes equations for an incompressible fluid written using the enthalpy formulation and assuming negligible viscous dissipation of mechanical energy [27]:

$$\frac{\partial u}{\partial r}+\frac{\partial v}{\partial z}+\frac{u}{r}=0, \tag{1a}$$

$$\rho\left(\frac{\partial u}{\partial t}+u\frac{\partial u}{\partial r}+v\frac{\partial u}{\partial z}\right)=-\frac{\partial p}{\partial r}+\frac{\partial \tau_{rr}}{\partial r}+\frac{\partial \tau_{rz}}{\partial z}+\frac{\tau_{rr}-\tau_{\varphi\varphi}}{r}+F_r, \tag{1b}$$

$$\rho\left(\frac{\partial v}{\partial t}+u\frac{\partial v}{\partial r}+v\frac{\partial v}{\partial z}\right)=-\frac{\partial p}{\partial z}+\frac{\partial \tau_{rz}}{\partial r}+\frac{\partial \tau_{zz}}{\partial z}+\frac{\tau_{rz}}{r}+F_z, \tag{1c}$$

$$\rho\left(\frac{\partial h}{\partial t}+u\frac{\partial h}{\partial r}+v\frac{\partial h}{\partial z}\right)=-\frac{\partial q_r}{\partial r}-\frac{\partial q_z}{\partial z}-\frac{q_r}{r}, \tag{1d}$$

where z is the height measured from the bottom of the film, u and v are the velocity components along Or and Oz axes, ρ, p, and h are the density, pressure, and specific enthalpy, τ_{rr}, τ_{zz}, $\tau_{\varphi\varphi}$, and τ_{rz}, are the components of the viscous stress tensor defined for the Newtonian fluid as

$$\tau_{rr}=2\mu\frac{\partial u}{\partial r},\quad \tau_{zz}=2\mu\frac{\partial v}{\partial z},\quad \tau_{\varphi\varphi}=2\mu\frac{u}{r},\quad \tau_{rz}=\mu\left(\frac{\partial u}{\partial r}+\frac{\partial v}{\partial z}\right), \tag{1e}$$

q_r and q_z are components of the heat flux vector defined by the Fourier law as

$$q_r=-\kappa\frac{\partial T}{\partial r},\quad q_z=-\kappa\frac{\partial T}{\partial z}, \tag{1f}$$

where T is the temperature, and μ and κ are the shear viscosity and thermal conductivity, respectively. Additional forces F_r and F_z in the momentum equation describe the gradual deceleration of the fluid in the two-phase region adjacent to the solid-liquid interface [27]:

$$F_r=-\frac{\mu}{K}u,\quad F_z=-\frac{\mu}{K}v. \tag{2a}$$

The permeability K is defined by the Kozeny-Carman equation, e.g. [26,27]:

$$K=K_0\frac{\phi^3}{(1-\phi)^2}, \tag{2b}$$

where K_0 is the permeability constant and ϕ is the volume fraction of liquid phase.

In the case of melting of binary alloys, the volume fractions of liquid and solid phases can be determined by the lever rule using the phase diagram of a binary system [27]. In the present study, which considers laser melting of pure aluminum targets, the volume fraction of liquid is defined based on temperature as follows:

$$\phi=\phi(T)=\begin{cases}0, & T<T_m-\Delta T;\\ s(\bar{\tau}(T)), & T_m-\Delta T\leqslant T\leqslant T_m+\Delta T;\\ 1, & T>T_m+\Delta T;\end{cases} \tag{3}$$

where T_m is the melting temperature of the target material, $\bar{\tau}(T)=[T-(T_m-\Delta T)]/2\Delta T$, ΔT is a numerical parameter, and $s(\bar{\tau})$ is chosen in the form of a cubic spline $s(\bar{\tau})=\bar{\tau}^2(3-2\bar{\tau})$ in order to ensure a smooth variation of all flow parameters in the vicinity of the melting isotherm $T=T_m$. Due to the finite value of ΔT, the solid-liquid interface in this model is replaced by a thin two-phase layer colored yellow in Fig. 1(b), where the volume fraction ϕ varies continuously from 0 at the solid side to 1 at the liquid side. The thickness of this layer is controlled by the value of ΔT and can be made sufficiently small by an appropriate choice of ΔT.

The equation of enthalpy for the two-phase system is introduced in the following form:

$$h(T)=\begin{cases}C_S T, & T<T_m-\Delta T;\\ h_{SL}(T), & T_m-\Delta T\leqslant T\leqslant T_m+\Delta T;\\ L_m+(C_S-C_L)T_m+C_L T, & T>T_m+\Delta T;\end{cases} \tag{4a}$$

where $h_{SL}(T)=c_0T_1+c_1T-c_2\cos\left(\frac{\pi}{2}\bar{\tau}(T)\right)+c_3\cos\left(\frac{\pi}{2}\bar{\tau}(T)\right)$, L_m is the latent heat of fusion of the target material, C_S and C_L are the specific heats of the solid and liquid phases, both assumed

to be temperature-independent, $c_0 = (C_S - C_L - L_m/\Delta T)/2$, $c_1 = (C_S + C_L + L_m/\Delta T)/2$, $c_2 = (C_S - C_L)\Delta T/\pi$, $c_3 = L_m/(2\pi)$, and $T_1 = T_m - \Delta T$. For pure solid and liquid phases, this equation coincides with the equations adopted, e.g., in Refs. [26,27]. The complicated representation of enthalpy in the two-phase region is chosen to ensure continuity of derivatives of h at the boundaries of the two-phase layer. Using the definition of the volume fraction given by Eq. (3) the viscosity and thermal conductivity of the two-phase medium are defined as follows [26,27]:

$$\mu(T) = (1 - \phi(T))\mu_S(T) + \phi(T)\mu_L(T), \tag{4b}$$

$$\kappa(T) = (1 - \phi(T))\kappa_S(T) + \phi(T)\kappa_L(T). \tag{4c}$$

Eqs. (1)–(4) are solved with the boundary conditions at the free surface accounting for changes of the shape of the liquid-vapor interface due to the inertia, recoil effect of vapor pressure, Marangoni effect, and material removal by evaporation. The thermal state of the free surface is defined by the absorption of the laser radiation, heat conduction in the target material, and thermal effect of evaporation. The absorption of the laser radiation is assumed to occur directly at the free surface, *BC* in Fig. 1(b), since the penetration depth of excimer or CO_2 laser in metals is of the order of 10 nm [7] and is substantially smaller than the typical length scale of temperature gradients generated by CW laser irradiation considered in the present paper. It is assumed that the irradiated film is placed in vacuum, so that the gas pressure above the film appears only as a result of evaporation of the film material.

The boundary conditions at the free surface include the following equations:

$$p_w - \tau_{wn} = p_e(T_w) - \sigma(T_w)\cos^3\theta\frac{\partial^2 H_w}{\partial r^2} \tag{5a}$$

– the equation of the normal stress balance, where p_w, T_w, and τ_{wn} are the surface pressure, temperature, and normal viscous stress, $p_e(T_w)$ and $\sigma(T_w)$ are the saturated vapor pressure and surface tension coefficient, and $\cos\theta = [1 + (\partial H_w/\partial r)^2]^{-1/2}$;

$$\tau_{w\tau} = \frac{d\sigma}{dT_w}\frac{\partial T_w}{\partial \tau} \tag{5b}$$

– the equation of the tangential stress balance, where $\tau_{w\tau}$ is the tangential viscous stress; and

$$\kappa(T_w)\frac{\partial T_w}{\partial n} = (1 - \mathcal{R})I(r,t)\cos\theta - L_b F_e(T_w) \tag{5c}$$

– the energy balance equation, where the first and second terms in the right-hand side account for the absorption of laser radiation with intensity $I(r,t)$ and cooling effect of evaporation, $\mathcal{R}$ is the reflectivity of the target material, and $F_e(T_w)$ is the mass flux density of the evaporated material, which is assumed to be defined by the Hertz-Knudsen model of evaporation [28]

$$F_e(T_w) = \frac{p_e(T_w)}{\sqrt{2\pi k_B N_a T_w/M}} \tag{6}$$

with the saturated vapor pressure of the target material $p_e(T_w)$ given by the Clapeyron-Clausius equation

$$p_e(T_w) = p_{0e}\exp\left[\frac{L_b M}{k_B N_a}\left(\frac{1}{T_{0e}} - \frac{1}{T_w}\right)\right]. \tag{7}$$

Here, k_B, N_a, and M are Boltzmann's constant, Avogadro constant, and molar mass of the target material, respectively, L_b is the latent heat of boiling, and p_{0e} is the saturated vapor pressure at a reference temperature T_{0e}. The first terms in the right-hand sides of Eqs. (5a) and (5b) are responsible for the recoil effect of vapor pressure and Marangoni effect, correspondingly. The surface tension coefficient is assumed to vary linearly with the local surface temperature, $\sigma(T_w) = \sigma_0 + \delta_\sigma(T_w - T_m)$ [18]. Spatial derivatives of temperature at the free surface in Eqs. (5b) and (5c) are calculated along the tangent and normal directions to the surface shown by vectors $\mathbf{t}_w$ and $\mathbf{n}_w$ in Fig. 1(b). The distribution of the CW laser intensity in the radial direction is assumed to be Gaussian,

$$I(r,t) = I_L\exp\left[-\log 2\left(\frac{r}{R_L}\right)^2\right], \tag{8}$$

where I_L is the laser intensity at the spot center and R_L is the full width at half maximum (FWHM) radius of the spot. The consideration in the present work is limited to sufficiently thin films, when $H_0/(2R_L) < 1$.

The height function $H_w(r,t)$ defining the shape of the irradiated surface evolves due to melt flow and evaporation and is calculated based on the evolutionary equation

$$\frac{\partial H_w}{\partial t} + u_w\frac{\partial H_w}{\partial r} = v_w - \frac{F_e(T_w)}{\rho\cos\theta}, \tag{9}$$

where u_w and v_w are the components of the fluid velocity at the free surface. Eq. (9) can be derived similarly to an equation describing the thickness of a film in the theory of thin film flows [29].

At the axis of symmetry *OC* the symmetry conditions are applied:

$$\text{At } r = 0: \quad u = 0, \quad \frac{\partial v}{\partial r} = 0, \quad \frac{\partial p}{\partial r} = 0, \quad \frac{\partial T}{\partial r} = 0, \quad \frac{\partial H_w}{\partial r} = 0. \tag{10}$$

The simulations are performed for free-standing films until their melting to the full depth, so that the bottom boundary *OA* is assumed to remain flat and thermally insulated in the course of a simulation. Thus, the following boundary conditions are applied at the bottom of the film:

$$\text{At } z = 0: \quad u = v = 0, \quad \frac{\partial p}{\partial z} = 0, \quad \frac{\partial T}{\partial z} = 0. \tag{11}$$

The lateral boundary *AB* is placed sufficiently far from the molten pool, so that not only the target material remains solid at this boundary but also the temperature increase due to heat transfer from the region of the laser energy deposition remains negligible up to $t < t_m$, where t_m is the melt-through time. Thus, the constant-temperature conditions for solid material are applied at this boundary:

$$\text{At } r = L_0 + L_1: \quad u = v = 0, \quad \frac{\partial p}{\partial r} = 0, \quad T = T_0, \quad H_w = H_0, \tag{12}$$

where T_0 is the initial temperature of the film at time $t = 0$.

The boundary value problem given by Eqs. (1)–(12) is solved for a film that has a uniform temperature $T_0 < T_m - \Delta T$ at the beginning of a simulation. All simulations are performed for aluminum targets irradiated by CW CO_2 laser with a wavelength of 9 μm. The material properties assumed in the simulations are listed in Table 1.

3. Numerical method for hydrodynamic simulations of CW laser melting

The hydrodynamic equations given by Eq. (1) are numerically solved on a computational mesh defined in the generalized coordinates $\xi = r/L_0$ and $\eta = y/H_w(r,t)$, which ensure the boundary-conforming coordinate transformation of the physical domain into a unit square. In addition, the coordinate η is transformed by an exponential function [30] in order to provide the refinement of the mesh towards the free surface (Fig. 2). In the transformed computational domain, a homogeneous rectangular computational mesh is introduced with N_ξ and N_η nodes along the ξ- and η-axis. Eq. (1) is solved on this mesh using the unsteady implicit pseudo-compressibility formulation proposed by Rogers and Kwak

Table 1
Properties of aluminum target used in simulations of CW laser melting adopted from Refs. [7,18,26,40].

Parameter	Value
Molar mass M	0.027 kg mole^{-1}
Density ρ	2700 kg m^{-3}
Specific heat of solid material C_S	900 J kg^{-1} K^{-1}
Thermal conductivity of solid material κ_S	238 W m^{-1} K^{-1}
Specific heat of liquid material C_L	1000 J kg^{-1} K^{-1}
Thermal conductivity of liquid material κ_L	107 W m^{-1} K^{-1}
Viscosity of liquid material μ_L, Ref. [39]	1.35×10^{-3} kg m^{-1} s^{-1}
Melting temperature T_m	933 K
Latent heat of fusion L_m	4.1×10^5 J kg^{-1}
Reference boiling temperature T_{0e}	2730 K
Reference boiling pressure p_{0e}	10^5 Pa
Latent heat of boiling L_b	10.75×10^6 J kg^{-1}
Surface tension coefficient σ_0 at $T_{0\sigma} = 300$ K, Ref. [18]	1.05 N m^{-1}
Gradient of surface tension coefficient δ_σ, Ref. [18]	-2.74×10^{-4} N m^{-1} K^{-1}
Permeability constant K_0, Ref. [26]	5×10^{-11}
Reflectivity $\mathcal{R}$ for laser wavelength 9 μm	0.97

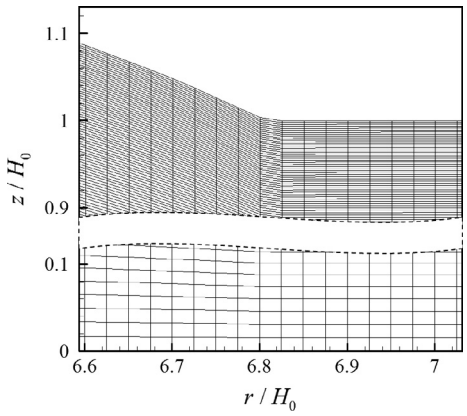

Fig. 2. Two small fragments of a computational mesh used for hydrodynamic simulations shown for a part of the computational domain outlined by the dashed rectangle in Fig. 1(b). The size of the computational mesh is uniform in the radial direction, but the vertical cell size decreases by 1–2 orders of magnitude from the bottom to the free surface of the film to ensure accurate representation of the velocity field with strong gradient in the vertical direction induced by the Marangoni stresses.

[31,32] and adopted in the present work for the system of the Navier-Stokes equations including the energy Eq. (1d). The convective terms in Eq. (1) are approximated with 5th order upwind difference operators [31,32], and the dissipative terms are approximated with standard central difference scheme of the 2nd order. Time derivatives in Eq. (1) are approximated with implicit 1st or 3rd order finite differences. Preliminary simulations reveal only a marginal difference between the numerical solutions obtained with these two approximations of time derivatives for the adopted values of the time step Δt.

The developed computational code was first applied to the lid-driven cavity problem and a good agreement with the literature data, e.g., [33,34], was established in the range of Reynolds number up to 2×10^4. In order to minimize errors in the conservation laws, especially in the continuity Eq. (1a), arising due to the boundary motion and approximation of equations on the moving mesh [35], the derivatives of the coordinate transformation functions are calculated numerically with central finite-difference approximations, while the Jacobian $J = \xi_x \eta_y - \xi_y \eta_x$ is calculated based on the numerical solution of the so-called geometric conservation law [35]:

$$\frac{\partial J}{\partial t} + \frac{\partial}{\partial \xi}\left(J \frac{\partial \xi}{\partial t}\right) + \frac{\partial}{\partial \eta}\left(J \frac{\partial \eta}{\partial t}\right) = 0. \tag{13}$$

Eq. (13) is approximated in the implicit form, similarly to Eq. (1), and solved together with the Navier-Stokes equations. The results of the simulations demonstrate that the use of Eq. (13) allows one to reduce the error in the total mass with respect to the mass of the molten material by about an order of magnitude, down to a typical value of 0.1% in the simulations described below in Section 5. The developed computational model, however, can be used only if the height function $H_w(r,t)$ remains sufficiently smooth in the course of simulation. The current implementation of the model is not capable of predicting the melt-through time under conditions when the rupture or spattering of the molten layer occurs before the target melts to the full depth.

The boundary conditions at the free surface, including Eq. (9) for the height function $H_w(r,t)$, are discretized in the implicit form using central differences of the 2nd order for derivatives along ξ and one-sided differences of the 1st order for derivatives along η. In order to find five unknown parameters, u_w, v_w, p_w, T_w, and H_w, in every computational node at the free surface Eqs. (5) and (9) are supplemented by the continuity equation, discretized in the boundary nodes.

In order to reduce the computational cost of the simulations, the whole computational domain is divided in the radial direction into two parts with lengths L_0 and L_1 (Fig. 1) chosen so that the film material remains solid at $r > L_0$. The full system of the Navier-Stokes equations is solved in the central part $OA'B'C$, i.e., for $r < L_0$, while only the heat conduction equation (Eq. (1d) with zero fluid velocity) is solved in the remaining part of the computational domain, $A'ABB'$. These two different models are solved on a single computation mesh common for the whole domain, ensuring a seamless coupling of the temperature fields in the two subdomains.

At each time step, the whole system of equations including discretized Eq. (1) and other equations representing the boundary conditions is solved iteratively until convergence. The iterative scheme for the solution of the linearized equations is based on the matrix Thomas algorithm [31] and is designed to provide the nodal values of temperature. The nodal values of enthalpy are calculated at the end of each time step based on the temperature field and Eq. (4a). This approach allows one to avoid the cumbersome calculation of temperature based on the nonlinear Eq. (4a).

The value of the pseudo-compressibility constant in the original formulation by Rogers and Kwak [31,32] was chosen individually for each simulation from the range from 1 to 10 depending on the largest anticipated melt velocities, so that the rate of convergences of iterations would be maximized. The value of the numerical parameter ΔT in Eqs. (3) and (4) was chosen to be 5 K, although only minor differences in the results were found from the simulations repeated with $\Delta T = 30$ K. The simulations were performed on computational meshes with $N_\xi = 201-2001$ and $N_\eta = 401-1001$ nodes. These numbers of nodes are much larger than those used in previous studies of Marangoni effect and recoil pressure induced melt flows in laser irradiated targets [14,20,26]. As explained in Section 5.1, the large number of nodes is necessary in order to accurately account for the melt flow in a thin surface layer affected by the thermocapillary stresses. A fragment of a typical computational mesh is shown in Fig. 2.

4. Simplified thermal models of CW laser melting

In this section we introduce a number of simplified thermal models of CW laser melting that can be used for quick evaluation of various characteristics of CW laser damage to thin metal films, such as the melt-through time t_m and the relative contribution of

various physical effects to the overall process of laser melting. The domains of applicability of the simplified models are established in Section 5 based on the comparison of their predictions with the results of hydrodynamic simulations.

As the first step in the development of the simplified models we consider simplifications of the full hydrodynamic model that still retain the explicit description of the molten material flow. In hydrodynamics, the simplified approaches to the solution of the full Navier-Stokes equations are well established for two limiting cases, namely, the Stokes (creeping) flows characterized by small Reynolds numbers, $Re \ll 1$, and the boundary layer flows characterized by high Reynolds numbers, $Re \gg 1$ (usually $Re > 10^3$) [36]. In the analysis of CW laser melting, the Reynolds number can be introduced based on the length scale of the laser spot in the form $Re = \rho U_* 2R_L/\mu_L$, where U_* is the characteristic flow velocity. Under typical conditions considered in the present study, U_* varies in the range from a few cm/s to a few m/s, e.g., see discussion of Fig. 6 in Section 5.1. Using properties of aluminum listed in Table 1, we obtain $Re = 4 \times 10^6 \times U_* R_L$ and, for the laser spots with $R_L \sim 0.1$—10 mm, Re varies from ~1 to ~10^4. Thus, one can see that moderate Reynolds numbers are typical for the CW laser melting problem, where neither the Stokes nor boundary layer approximations can be used. Although at the upper limit of this range the boundary layer approximation could still be formally applicable, other factors can preclude the consideration of the molted pool flow as a boundary layer. In particular, the boundary layer approximation is not capable of describing flows with circulating zones, while the circulating zones are common for thermocapillary flows, e.g., see fields of melt velocity shown in Fig. 6 in Section 5.1. The boundary layer approximation and its further simplification in the form of a thin film flow [29] can only describe melting of very thin films or pulsed laser melting of extremely thin surface layers, as it was suggested in Refs. [19,25].

4.1. Two-dimensional thermal model of laser melting

As a way to evaluate the contribution of the melt flow to the CW laser melting process, we compare predictions of hydrodynamic models with a simple two-dimensional thermal model, where only the temperature field is calculated based on the energy Eq. (1d), and fluid flow is neglected, i.e.,

$$\rho \frac{\partial h}{\partial t} = -\frac{\partial q_r}{\partial r} - \frac{\partial q_z}{\partial z} - \frac{q_r}{r}. \tag{14}$$

This equation is solved together with Eq. (9) for the interface shape function $H_w(r,t)$ with $u_w = 0$ using the same implicit numerical approach as described in Section 3 for the full Navier-Stokes equations. The boundary conditions for this equation can be obtained based on the boundary conditions for enthalpy given by Eqs. (5c) and (10)–(12) assuming zero flow velocity and viscous stresses. This model is further referred to as 2D thermal model of laser melting.

4.2. One-dimensional thermal model of laser melting accounting for the melt expulsion

If the size of the laser spot is large enough or the film thickness is small, then the temperature distribution along the spot axis can be largely unaffected by heat conduction in the radial direction during the whole process of melting of the film. Such conditions make sense in the present work, since the consideration is limited to the case of $H_0/(2R_L) < 1$. Then, assuming $q_r = 0$, one can reduce Eq. (14) to a 1D heat conduction equation with respect to the distribution of temperature $T(z,t)$ along the axis of the laser beam. In the present paper, we use the front tracking method to solve this 1D heat conduction equation with moving sharp solid-liquid and liquid-vapor interfaces (Fig. 3). For this purpose, we write the heat conduction equation separately for solid and liquid phases in the form

$$\rho C_\alpha \frac{\partial T_\alpha}{\partial t} = \frac{\partial}{\partial z}\left(\kappa_\alpha \frac{\partial T_\alpha}{\partial z}\right), \tag{15}$$

where subscript "α" denotes parameters of different phases, with $\alpha = S$ for solid and $\alpha = L$ for liquid phases. Eq. (15) is solved together with the equations of motion of the liquid-vapor (at $z = Z_{LV}(t)$) and solid-liquid (at $z = Z_{SL}(t)$) interfaces,

$$\frac{dZ_{LV}}{dt} = -U_{LV}, \quad \frac{dZ_{SL}}{dt} = -U_{SL}, \tag{16}$$

where U_{LV} and U_{SL} are the corresponding interface velocities. It is assumed that both evaporation and melt expulsion contribute to the motion of the free surface, while the Marangoni effect is neglected, so that

$$U_{LV} = U_{LV(e)} + U_{LV(\exp)}, \tag{17a}$$

where $U_{LV(e)}$ and $U_{LV(\exp)}$ are the contributions from evaporation and material expulsion, respectively. The rate of evaporation is assumed to be defined by the Hertz-Knudsen model of evaporation, Eq. (6), so that $U_{LV(e)}$ takes the form

$$U_{LV(e)} = \frac{p_e(T_w)}{\rho\sqrt{2\pi k_B N_a T_w/M}}, \tag{17b}$$

where $T_w = T_L(Z_{LV}(t),t)$. In order to calculate the second term in the right-hand side of Eq. (17a), we follow the idea of Ref. [13] and estimate $U_{LV(\exp)}$ based on the Bernoulli integral, assuming that the molten pool has a shape of a cylindrical slab of the radius coinciding with the radius of the laser spot R_L and thickness $H_m = Z_{LV}(t) - Z_{SL}(t)$ (Fig. 3). The fluid velocity and pressure at the vapor-liquid interface, $U_{LV(\exp)}$ and $p_e(T_w)$, and velocity and pressure at the lateral surface of the cylinder, U and p, can be connected to each other by the Bernoulli integral, $\rho U_{LV(\exp)}^2/2 + p_e(T_w) = \rho U^2/2 + p$, and the mass conservation law, $\pi R_L^2 U_{LV(\exp)} = 2\pi R_L H_m U$. Taking into account that at the lateral surface $p \ll p_e(T_w)$ and, thus, p can be assumed to be equal to zero, one can derive an equation

$$U_{LV(\exp)} = \frac{2H_m/R_L}{\sqrt{1-(2H_m/R_L)^2}}\sqrt{\frac{2p_e(T_w)}{\rho}}. \tag{17c}$$

For the purpose of conciseness, hereinafter the contribution of the melt expulsion to the surface recession velocity at the center of laser spot, $U_{LV(\exp)}$, is referred to as the melt expulsion velocity. Eq. (17c) predicts that the magnitude of the melt expulsion velocity essentially depends not only on the surface temperature T_w, but also on the thickness of the molten layer H_m. It means, in particular, that for small H_m the melt expulsion velocity $U_{LV(\exp)}$ can be small even if T_w is large. This equation is applicable only if $2H_m/R_L < 1$, i.e. only if the molten layer is sufficiently thin. Simulations and analysis made with the steady-state analog of this model (Section 4.2) show that if R_L is fixed, then H_m increases with decreasing I_L and eventually becomes larger than R_L. Thus, for each R_L there is a minimum value I_L below which the 1D thermal model including Eq. (17c) cannot be used.

Velocity U_{SL} is defined by the Stefan condition at the solid-liquid interface:

$$T_S(Z_{SL},t) = T_L(Z_{SL},t) = T_m, \quad \rho L_m U_{SL} = \left(\kappa_S \frac{\partial T_S}{\partial z} - \kappa_L \frac{\partial T_L}{\partial z}\right)\Big|_{z=Z_{SL}}. \tag{18}$$

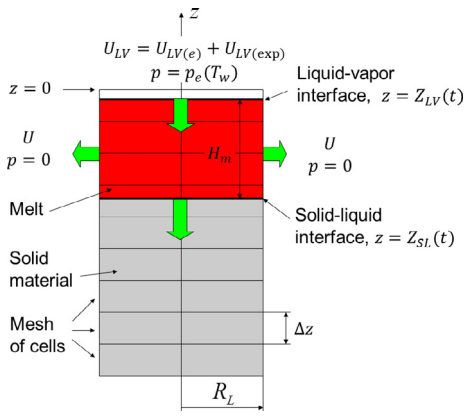

Fig. 3. Sketch of the computational setup used in calculations of the CW laser heating and melting of a target material based on the 1D thermal model. The heat transfer equations for solid (gray) and liquid (red) parts of the system are solved with the immersed boundary method on a fixed mesh of cells, while the solid-liquid and liquid-vapor interfaces move with respect to cells in the course of a simulation. (For interpretation of the references to color in this figure legend, the reader is referred to the web version of this article.)

Eqs. (15)–(18) are solved with the boundary condition of energy balance at the free surface, Eq. (5c), which for the present 1D case takes the form

$$\kappa(T_L)\frac{\partial T_L}{\partial z}\bigg|_{z=Z_{LV}} = (1-\mathcal{R})I_L - L_b\rho U_{LV(e)}, \tag{19}$$

and the boundary condition at the bottom boundary of the film, which is assumed to be thermally insulated, i.e.,

$$\frac{\partial T_S}{\partial z}\bigg|_{z=0} = 0. \tag{20}$$

1D thermal models based on Eq. (15) with $U_{LV} = U_{LV(e)}$ are extensively used in the analysis of both CW and pulsed laser ablation [7]. It will be shown below that the additional term given by Eqs. (17c) allows one to satisfactory predict the overall recoil effect of the vapor pressure on the motion of the free surface of the molten material.

The 1D thermal model given by Eqs. (15)–(20) is implemented numerically with the immersed boundary method, e.g. [37]. Eq. (15) is solved with 2nd order approximation of spatial derivatives on a fixed homogeneous computational mesh. In the course of a simulation, the interfaces move with respect to cells of the mesh, and parameters at the interfaces along with temperature derivatives at the nodes of the computational mesh adjacent to the interfaces are calculated based on one-side linear interpolation of temperature within the solid and liquid phases. The Fortran code HPLA1D.f90 implementing this model can be downloaded from [38].

The results obtained with the 1D thermal model for a 1-cm-thick aluminum film irradiated by a CW laser at different laser intensities I_L are shown in Fig. 4. To highlight the role of melt expulsion on the melting process, the calculations are also performed with a simplified model where the contribution of the melt expulsion velocity to the motion of the free surface is neglected, i.e., $U_{LV(\exp)} = 0$. The comparison of results obtained with (solid curves) and without (dashed curves) melt expulsion shows that the process of melting can be divided into three stages. At the first *pre-melting* stage of duration τ_{pm} the surface temperature remains smaller than the melting temperature of the target material. At the second *waiting* stage of duration τ_d the molten layer appears, but its thickness and surface temperature remain too small to develop a substantial melt expulsion velocity, so that the results obtained with and without the expulsion closely coincide with each other. The duration of this stage τ_d, indicated in Fig. 4(a) for $I_L = 10^6$ W cm^{-2}, is farther referred to as the delay time, while the time corresponding to the onset of the expulsion, $t_e = \tau_{pm} + \tau_d$, is referred to as the expulsion waiting time. This stage is followed by the third *expulsion* stage, where the expulsion affects the way further melting of the film proceeds, resulting in a decrease of the surface temperature, thickness of the molten layer, and the melt-through time t_m, as well as in an increase of the melting front propagation velocity as compared to the results obtained with a model that neglects expulsion. The behavior of T_w, H_m, and U_{LS} versus time drastically changes at the beginning of the expulsion stage: U_{LS} rises very fact at the end of the waiting stage, and then T_w, H_m, and U_{LS} tend to approach certain constant, time-independent values. This is clearly seen in Fig. 4 for $I_L \gtrsim 10^6$ W cm^{-2}. At smaller intensities, the expulsion stage for the film of a finite thickness is getting shorter or can be absent at all, as melting of the film to the full depth may occurs prior to reaching the asymptotical, time-independent values of the process parameters.

The time, corresponding to the onset of melt expulsion at different I_L, is indicated in Fig. 4 by dash-dotted lines. It is important to note that the expulsion stage begins at different values of surface temperature, which increases with increasing I_L. This observation can be explained by the effect of H_m on the melt expulsion velocity predicted by Eq. (17c). With increasing I_L, the thickness of the molten layer H_m decreases (Fig. 4(b)) and, as can be seen from Eq. (17c), the same melt expulsion velocity requires higher values of the surface temperature. The decrease of H_m is, in turn, explained by the Stefan condition, Eq. (18), at the melting front: An increase in the melting front velocity requires a rise in the temperature gradient within the molten layer, $|\partial T_L/\partial z| \sim (T_w - T_m)/H_m$, which occurs due to increase in $T_w - T_m$, and decrease in H_m.

All these findings, revealed with the 1D thermal model supplemented by Eq. (17c) accounting for melt expulsion, are in a good qualitative (and, for sufficiently large I_L, quantitative) agreement with the results of direct numerical simulations performed with the hydrodynamic model of laser melting and described in Section 5.

4.3. Steady-state solution of the 1D thermal model for a bulk target

In a bulk target, the 1D thermal model described in Section 4.1 yields a solution where both the solid-liquid and liquid-vapor interfaces move with a constant velocity $U_{SL} = U_{LV} = const$. This is the steady-state solution in the frame of reference moving together with interfaces. It establishes after an initial transient stage and fully describes the subsequent process of 1D CW melting in a bulk target. The existence of such steady-state solutions for the case when material removal is driven only by the surface evaporation is well-known, e.g. [7]. In the present work, the steady-state solution is considered assuming temperature-independent thermal conductivities and specific heats of both solid and liquid phases. The novel element of the present model is the inclusion of the melt expulsion described by Eq. (17c). For films of sufficiently large but finite thickness, the obtained solution can describe an intermediate stage of meting, when the melting front is far from both the free surface and the bottom of the film. The existence of such quasi-steady-state stage of melting, when the surface temperature, thickness of the molten layer, and melting front velocity remain approximately constant, can be seen from Fig. 4 for $I_L \gtrsim 10^6$ W cm^{-2}.

In order to formulate the problem in the steady-state form, one can rewrite Eqs. (15)–(20) for a bulk target in a frame of reference, which moves with a constant interface velocity $U_{LV} = U_{SL}$ and

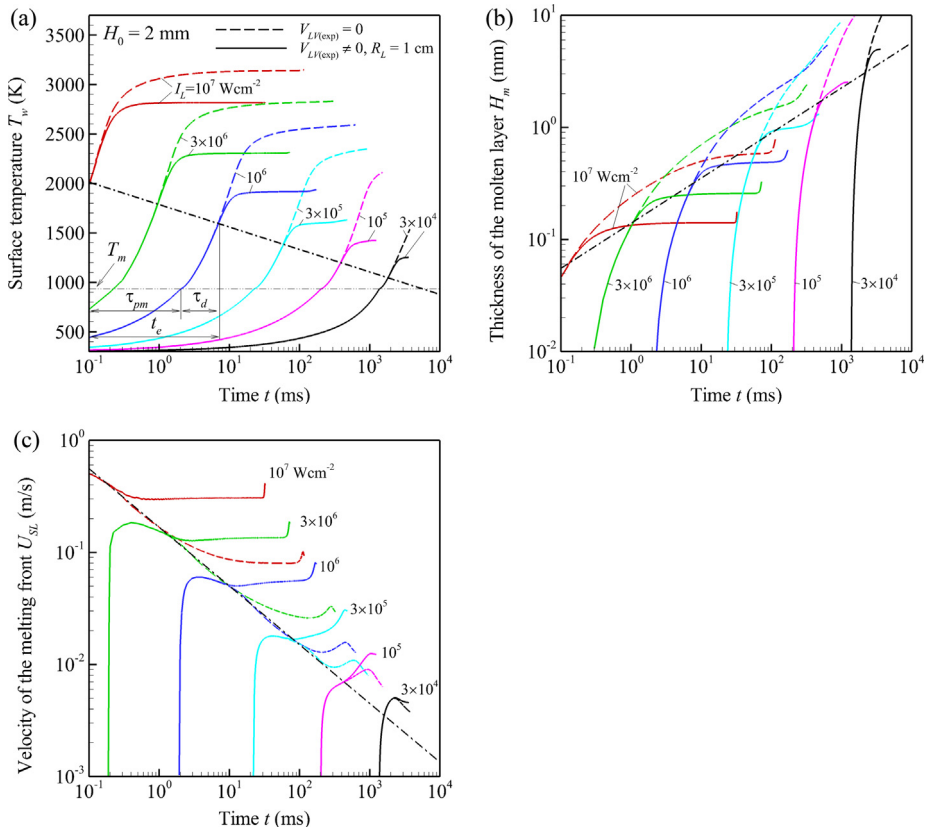

Fig. 4. Surface temperature T_w (a), thickness of the molten layer H_m (b), and its velocity U_{SL} (c) versus time t obtained with 1D thermal model of CW laser heating of an aluminum film of thickness $H_0 = 1$ cm with (solid curves) and without (dashed curves) the melt expulsion described by Eq. (17c) included in the model. The simulations are performed for laser intensities I_L indicted in the figure panels. The laser spot radius $R_L = 1$ cm is assumed in the melt expulsion calculations. In panel (a), the horizontal dash-double-dotted line corresponds to the melting temperature T_m, and τ_d is the delay time between the onsets of melting at $t = \tau_{mp}$ and expulsion at $t = t_e$. The dash-dotted lines approximately show the conditions for the onset of the melt expulsion at various I_L. The right-most point of each curve corresponds to the melt-through time t_m.

where the new coordinate $\bar{z}$ is related to the coordinate z in the laboratory frame of reference as $\bar{z} = z - U_{LV}t$. Assuming that $\partial T_\alpha/\partial t = 0$ and $\bar{z} = 0$ corresponds to the liquid-vapor interface, one can then obtain the following equations for the steady-state temperature fields $T_\alpha(\bar{z})$

$$\frac{\partial}{\partial \bar{z}}\left(\kappa_\alpha \frac{\partial T_\alpha}{\partial \bar{z}} + \rho C_\alpha U_{SL} T_\alpha\right) = 0, \tag{21}$$

(similar to Eq. (15), subscript "α" denotes parameters of different phases), which should be solved with conditions of the energy balance at the liquid-vapor interface,

$$\kappa_L \frac{\partial T_L}{\partial \bar{z}}\bigg|_{\bar{z}=0} = (1-\mathcal{R})I_L - L_b \rho U_{LV(e)}, \tag{22}$$

Stefan condition at solid-liquid interface

$$T_S(-H_m) = T_L(-H_m) = T_m, \quad \rho L_m U_{SL} = \left(\kappa_S \frac{\partial T_S}{\partial \bar{z}} - \kappa_L \frac{\partial T_L}{\partial \bar{z}}\right)\bigg|_{\bar{z}} = -H_m, \tag{23}$$

and condition at infinitely large depth

$$T(\bar{z}) \to T_0 \quad \text{at} \quad \bar{z} \to \infty. \tag{24}$$

The solution of Eq. (21) takes the form

$$T_S(\bar{z}) = T_0 + (T_m - T_0)\exp\left[-\frac{\rho C_S U_{SL}}{\kappa_S}(\bar{z} + H_m)\right], \tag{25a}$$

$$T_L(\bar{z}) = T_1 + (T_m - T_1)\exp\left[-\frac{\rho C_L U_{SL}}{\kappa_L}(\bar{z} + H_m)\right], \tag{25b}$$

where $T_1 = T_m - [C_S(T_m - T_0) + L_m]/C_L$. Using these temperature distributions and assuming that the interface velocity is given by Eq. (17), one can reduce the boundary conditions to a system of two equations with respect to the surface temperature T_w and thickness of the molten layer H_m:

$$\rho C_L[U_{LV(e)}(T_w) + U_{LV(\exp)}(T_w, H_m)](T_w - T_1) + \rho L_b U_{LV(e)} = (1-\mathcal{R})I_L, \tag{26a}$$

$$T_w - T_1 = (T_m - T_1)\exp\left[-\frac{\rho C_L[U_{LV(e)}(T_w) + U_{LV(\exp)}(T_w, H_m)]H_m}{\kappa_L}\right]. \tag{26b}$$

In the present work, the non-linear Eq. (26) is solved iteratively using the Newton-Raphson method. The Fortran code HPLA1DSS.f90 implementing this model can be downloaded from [38].

The surface temperature, thickness of the molten layer, and interface velocity calculated based on Eq. (26) for a range of laser intensities and several laser spot radii are shown in Fig. 5. The steady-state values of T_w and H_m are in a good agreement with values obtained based on the unsteady 1D thermal model for the quasi-steady-state stage of the melting process (Fig. 4). The steady-state model predicts the dominant effect of melt expulsion at $I_L < 10^6$ W cm^{-2}, when it makes an order of magnitude larger contribution to the velocity of the liquid-vapor interface as compared to evaporation. A decrease in the laser spot size enhances the effect of the expulsion and substantially reduces the surface temperature and thickness of the molten layer at a given I_L. The thickness of the molten layer, however, decreases with decreasing

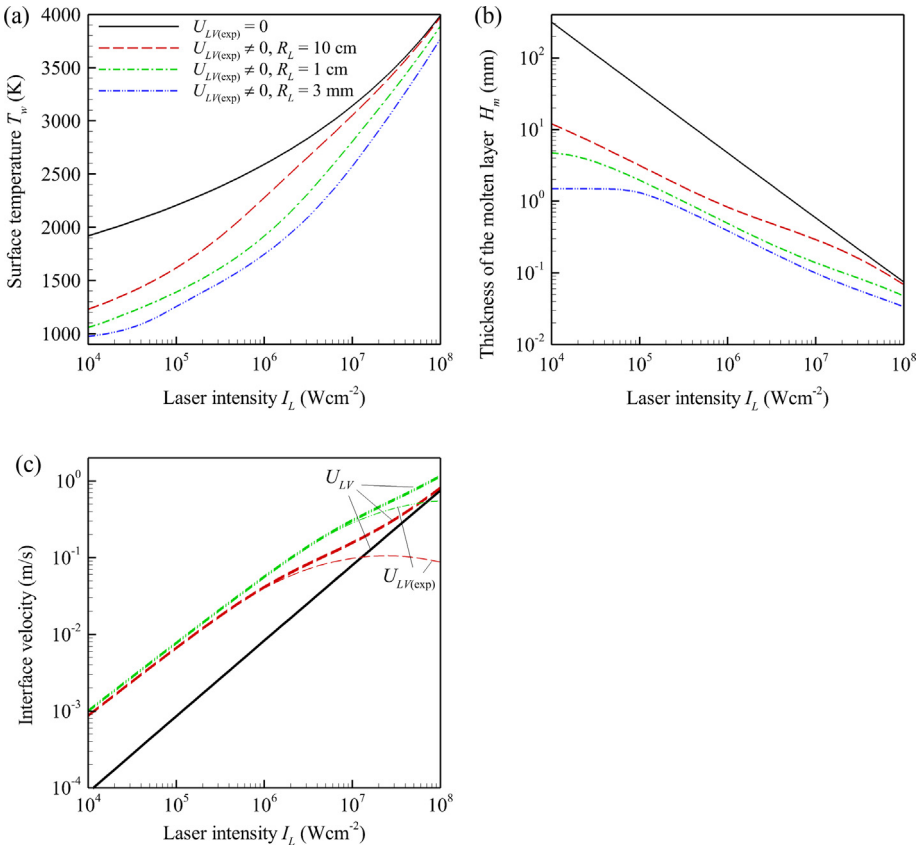

Fig. 5. Surface temperature T_w (a), thickness of the molten layer H_m (b), and the interface velocity (c) versus laser intensity I_L calculated with the 1D steady-state thermal model without the melt expulsion ($U_{LV(exp)} = 0$, solid curves), and with the expulsion described by Eq. (17c) for the laser spot radii R_L of 10 cm (dashed curves), 1 cm (dash-dotted curves), and 3 mm (dash-double-dotted curves). In panel (c), thick curves correspond to the total interface velocity U_{LV}, while the thin curves correspond to the contribution of the expulsion velocity $U_{LV(exp)}$. For clarity, results for $R_L = 3$ mm are not shown in panel (c).

R_L much slower than R_L itself, so that $2H_m/R_L$ eventually becomes larger than 1 and calculations based on Eqs. (17c) become impossible. For $I_L = 10^4$ W cm^{-2}, this limit of applicability of Eq. (17c) is reached for R_L that is between 2 mm and 3 mm.

With increasing I_L, the surface temperature rises leading to the corresponding increase in the intensity of evaporation. At the upper limit of the considered range of I_L, the surface temperature becomes so high that the material removal process is dominated by evaporation, while the contribution of melt expulsion becomes less important, especially for large spot radii, as can be seen from the comparison of corresponding thick and thin curves in Fig. 5(c). The increase in the laser intensity also leads to a strong decrease in the thickness of the molten layer, Fig. 5(b), since, according to Eq. (23), the increasing interface velocity should be supported by the increasing temperature gradient across the molten layer.

5. Results of hydrodynamic simulations and comparison to simplified models

The hydrodynamic simulations of CW laser melting of aluminum films were performed for laser spots of two different sizes: A large spot of $R_L = 1$ cm, which is typical for laser damage applications [2,3,5], and a small spot of $R_L = 0.1$ mm, which is characteristic of material processing with CW lasers, e.g. [4,6]. The results of the simulations performed with and without the recoil pressure and Marangoni effects are systematically compared with the simplified models of laser melting introduced in Section 4. The discussion of the simulation results is focused on establishing the major processes controlling the melt-through time, and revealing the predictive abilities and limitations of the simplified models.

5.1. Large laser spot size

Simulations for the laser spot size $R_L = 1$ cm were performed for aluminum films with thicknesses of $H_0 = 1$—4 mm in the range of laser intensities I_L from 3×10^4 W cm^{-2} to 3×10^6 W cm^{-2}. This range of I_L was chosen based on the preliminary results obtained for similar conditions with the 1D thermal model discussed in Section 4.2. The radial size of the computational domain was equal to $L_0 = L_1 = 2$ cm and the time step was $\Delta t = 0.01$—0.001 ns.

The simulations predict strong increase in the maximum magnitude of the radial velocity due to the Marangoni stresses. For instance, at a relatively low $I_L = 10^5$ W cm^{-2}, the Marangoni stresses induce four orders of magnitude larger maximum radial velocity then in the case of the flow driven by the recoil effect only (Fig. 6). This large radial velocity initially appears only in a thin surface layer, which then gradually spreads into the depth with time as it is seen from the distributions of radial velocity shown for two target cross sections in Fig. 6(d). The thickening rate increases with increasing viscosity of the molten material and, in the present simulations, is limited by relatively low viscosity of liquid aluminum [39]. The small thickness of the layer affected by the Marangoni stresses is the major factor that requires the use of a large number of nodes in the computational mesh, as well as the computational mesh refinement close to the free surface illustrated in Fig. 2. The fine mesh, in turn, reduces the maximum time step that can be used in the calculations and increases the

computational cost of the simulations. It is worth noting that the computational meshes used for similar simulations in Refs. [20,26] have much smaller number of nodes than in the present study and are not capable of accurate description of the flow field in the layer affected by the Marangoni stresses. Large spacing between nodes in the computational mesh results in an excessive artificial viscosity and, consequently, overestimation of the Marangoni effect.

The Marangoni stresses also qualitatively change the whole pattern of melt flow. In the case when Marangoni stresses are not accounted for in the model, purely radial outflow, where the radial velocity is positive everywhere and vorticity is small, occurs. The Marangoni stresses, on the contrary, result in shear flow close to the free surface and induce the formation of a circulating zone in the molten pool with strong vorticity. Such circulating flows can be calculated with neither the boundary layer nor thin film approximations.

Due to the small thickness of the layer affected by the Marangoni stresses, their overall effect on the shape of the molten pool is marginal and the melt-through time in the simulations illustrated by Fig. 6 decreases due to Marangoni stresses only from 229 ms to 228 ms, i.e. less than by 0.5%. At larger I_L, the Marangoni stresses produce more prominent changes in the shape of the free surface and increase the radial size of the molten pool (Figs. 7 and 8). The effect of the Marangoni stresses on the evolution of the free surface temperature, thickness of the molten layer at the spot axis (Fig. 9), and the melt-through time, however, remains small in the whole range of I_L considered in this study. With increasing I_L, the radial velocity due to the recoil effect of vapor pressure increases sharply, while the additional flow acceleration of the liquid material induced by the Marangoni stresses remains limited, as it is seen, e.g., from comparison of Fig. 8(a) and (b) obtained for $I_L = 6 \times 10^5$ W cm^{-2} with and without Marangoni stresses. This makes the Marangoni effect to be inefficient in reducing the melt-through time at any I_L.

In order to reveal the contribution of the latent heat of melting as well as the recoil and Marangoni effects on the melt-through time and the evolution of the thickness of the molten layer, a series of simulations was performed with five different models of laser melting (Fig. 9). The predictions of the two-phase 1D thermal model (solid curves), where melt expulsion is accounted for with Eq. (17c), are in a good agreement with the results of full hydrodynamic simulations (dash-dotted and dash-double-dotted curves). Among other thermal models, the 1D model provides the best agreement with the results of hydrodynamic simulations in terms of T_w, H_m, and t_m. The 2D thermal model where the latent heat of melting is not accounted for (short-dash curves) underestimates the melt-through time by roughly a factor of two. The 2D thermal model where the thermal energy transformation into the latent heat of melting is accounted for (long-dash curves) substantially overestimated the terminal surface temperature and melt-through time as compared to the hydrodynamic models. The hydrodynamic models with and without the Marangoni effect predict almost identical final surface temperature and the melt-through time.

The results presented in Fig. 9 demonstrate that, under conditions when melt expulsion due to the recoil pressure affects the melt-through time, the whole process of melting can be divided into three distinct stages previously established in Section 4.2 based on the analysis of the simulation results obtained with the 1D thermal model. Surface melting starts at about $t = 2$ ms, signifying the transition from the pre-melting to the waiting stage of the process. The transition from the waiting to the expulsion stage is marked by the change in the slope of the dash-dotted and dash-double-dotted curves at about $t = 10$ ms. During the waiting stage, an increase in the thickness of the molten later and surface temperature occurs relatively fast and is well described by both the 1D and 2D two-phase thermal models. This is an indication of that at this stage melt flow is not well developed yet. At the third (expulsion) stage, the surface temperature remains almost constant and the thickness of the molten layer slowly increases with time. At this stage, expulsion of liquid from the central part of the laser spot keeps the surface temperature there at a constant level. The time between the onset of melting at $t = 2$ ms and the onset of melt expulsion at $t = 10$ ms is the delay time τ_d, which was previously identified in simulations based on the 1D thermal model (Fig. 4). The Marangoni stresses cause faster acceleration of the melt in a thin surface layer of the film, which results in a smoother transition between the waiting and expulsion stages. The overall effect of the Marangoni stresses on the evolution of the surface temperature and thickness of the molten layer, though, is relatively small. The results obtained with the hydrodynamic models are in a close quantitative agreement with results of 1D thermal model (Fig. 4), where the recoil effect is accounted for with Eq. (17c). The delay time, final surface temperature, thickness of the molten layer, and melt-through time predicted with the 1D thermal model are almost identical to the ones obtained with the full hydrodynamic model.

The dependence of the shape of the molten pool at $t = t_m$ on laser intensity I_L is illustrated in Fig. 10. In the range of I_L considered in these simulations, the material removal due to evaporation plays only a marginal role (see, e.g., Fig. 5(c), where the total interface velocity coincides with the contribution of the melt expulsion velocity for $I_L \leqslant 10^7$ W cm^{-2} and the spot radius $R_L = 1$ cm). Thus, the shape of the free surface is primarily affected by the effect of recoil from the evaporation process. These results, therefore, demonstrate the existence of a range of irradiation conditions where the evaporation is too weak to cause any significant material removal, but strong enough to drive a substantial expulsion of the melt from the center of the laser spot. With increasing I_L, the melt propagates farther away from the spot center, reaching, e.g., the distance of $r = 1.9R_L$ at $I_L \leqslant 2 \times 10^6$ W cm^{-2} (Fig. 10(f)). The total mass of the melt at $t = t_m$ also increases with increasing I_L, which is obvious from the comparison of the shapes of solid-liquid interface, although this dependence is not very strong. As was already mentioned above, at the expulsion stage the thickness of the molten layer increases rather slowly with time, so that the propagation of the melting front towards the bottom of the film occurs in a quasi-steady state manner. The results presented in Fig. 10 are obtained by the time of melting of the film to the full depth at the center of the laser spot and, thus, they do not represent the final shape of the free surface that would form after solidification of the molten pool. Nevertheless, the formation of a pronounced rim raising above the original level of the irradiated surface of the film can be inferred from the simulation results.

With further increase in the laser intensity above the maximum I_L considered in Fig. 10, the shape of the free surface of the molten pool undergoes strong oscillations. The first signs of the oscillations, which eventually affect the whole molten pool and the shape of the solid-liquid interface, are already visible in Fig. 10(e) and (f). The processes responsible for the development of these oscillations can be analyzed based on the results of a simulation performed at $I_L = 3 \times 10^6$ W cm^{-2} and illustrated in Fig. 11. In this case, the adsorbed laser power is sufficiently high to induce the fast formation of a thin molten layer within a region extending beyond R_L (Fig. 11(a)). The temperature distribution across the molten pool is strongly nonhomogeneous: At the center of the laser spot the temperature and vapor pressure are high enough to induce almost immediate fluid flow in the radial direction, whereas at the periphery of the molten pool the vapor pressure is low, and much longer

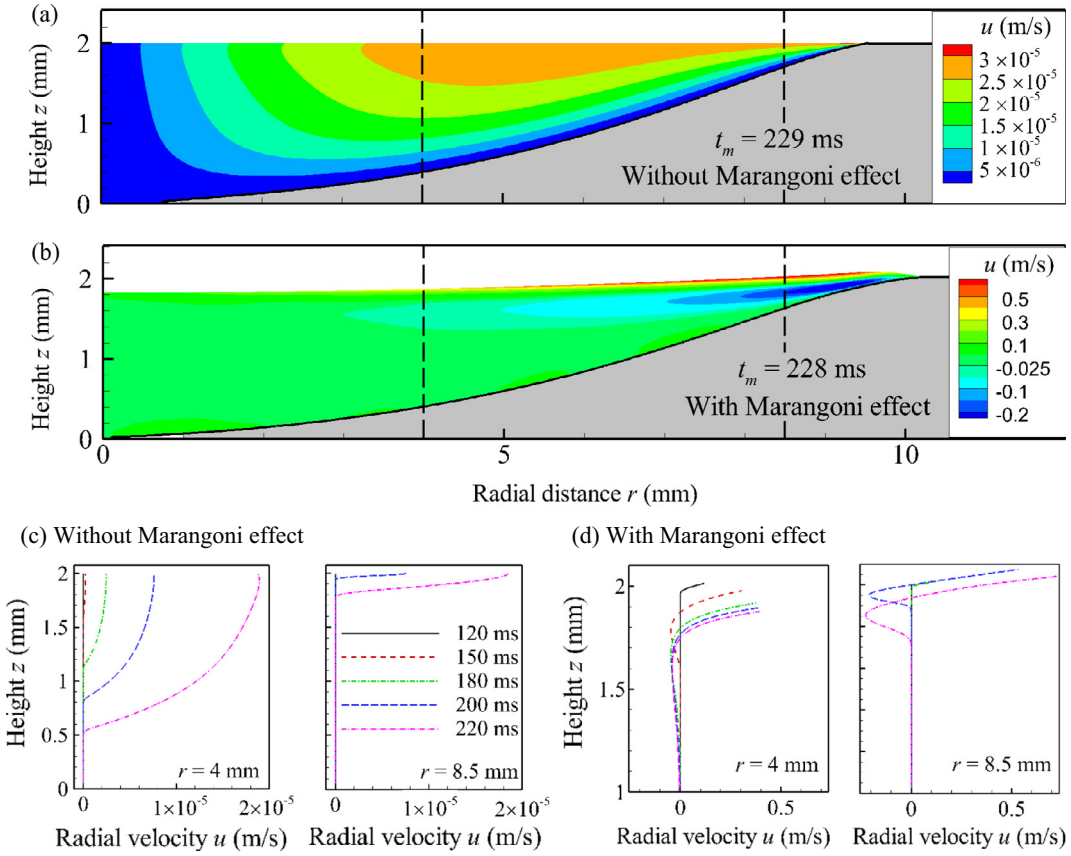

Fig. 6. Fields of radial velocity u (a, b) obtained by the time $t = t_m$ and distributions of radial velocity in the cross sections at $r = 4$ mm and $r = 8.5$ mm (c, d) obtained in hydrodynamic simulations performed with the recoil pressure effect only (a, c), and with both the recoil and Marangoni effects (b, d) for a film thickness $H_0 = 2$ mm, FWHM spot radius $R_L = 1$ cm, and laser intensity $I_L = 10^5$ W cm^{-2}. In panels (a) and (b), black curves mark the positions of solid-liquid interfaces where $T = T_m$, gray areas correspond to the solid material, and dashed lines mark the positions of the cross sections used for panels (c) and (d). The melt-through time t_m is indicated on panels (a, b). In panels (c) and (d), the radial velocity distributions are plotted for several moments of times indicated in panel (c).

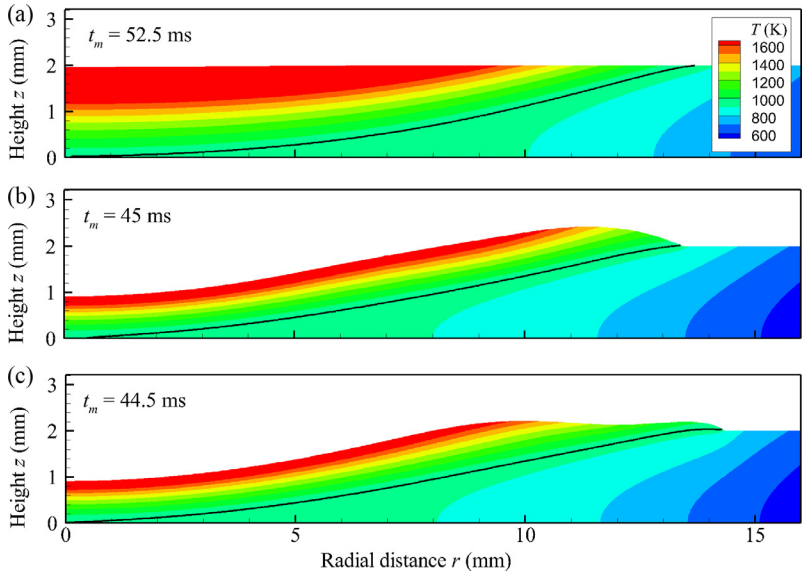

Fig. 7. Fields of temperature T obtained for the time $t = t_m$ with models that do not allow for any fluid flow (a), account for the melt flow driven by the recoil pressure effect (b), and include both the recoil pressure and Marangoni effects (c). All three simulations are done for the film thickness $H_0 = 2$ mm, FWHM spot radius $R_L = 1$ cm, and laser intensity $I_L = 6 \times 10^5$ W cm^{-2}. The black curves mark the positions of solid-liquid interfaces where $T = T_m$. The melt-through time t_m is indicated in the figure panels.

time is required in order to induce the radial motion of the fluid. The large mismatch in the radial velocities between the almost stationary melt in the surface layer at the periphery of the molten pool and the rapidly advancing melt expelled from the central part of the pool leads to the appearance of a wave propagating towards the edge of the molten pool (Fig. 11(b, c)). The development of instabilities in the course of the wave propagation and its interaction with the edge of the molted pool results in the formation of an

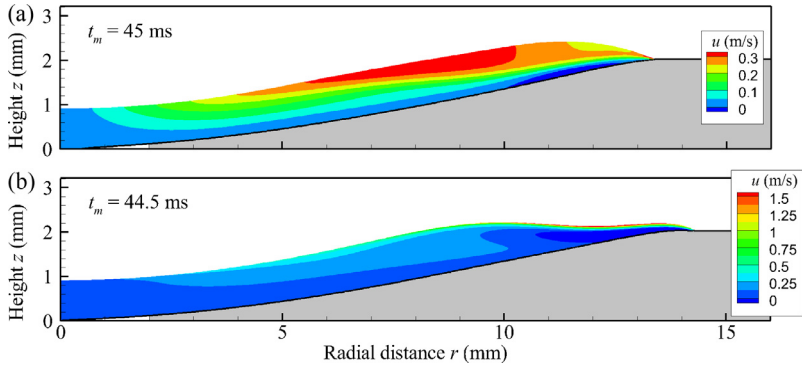

Fig. 8. Fields of radial velocity u obtained for the time $t = t_m$ in the hydrodynamic simulations accounting for the recoil pressure effect (a) and both the recoil pressure and Marangoni effects (b). The simulations are performed for the film thickness $H_0 = 2$ mm, FWHM spot radius $R_L = 1$ cm, and laser intensity $I_L = 6 \times 10^5$ W cm^{-2}. The blacks curves mark the positions of solid-liquid interfaces where $T = T_m$ and the gray areas correspond to the solid material. The melt-through time t_m is indicated in the figure panels.

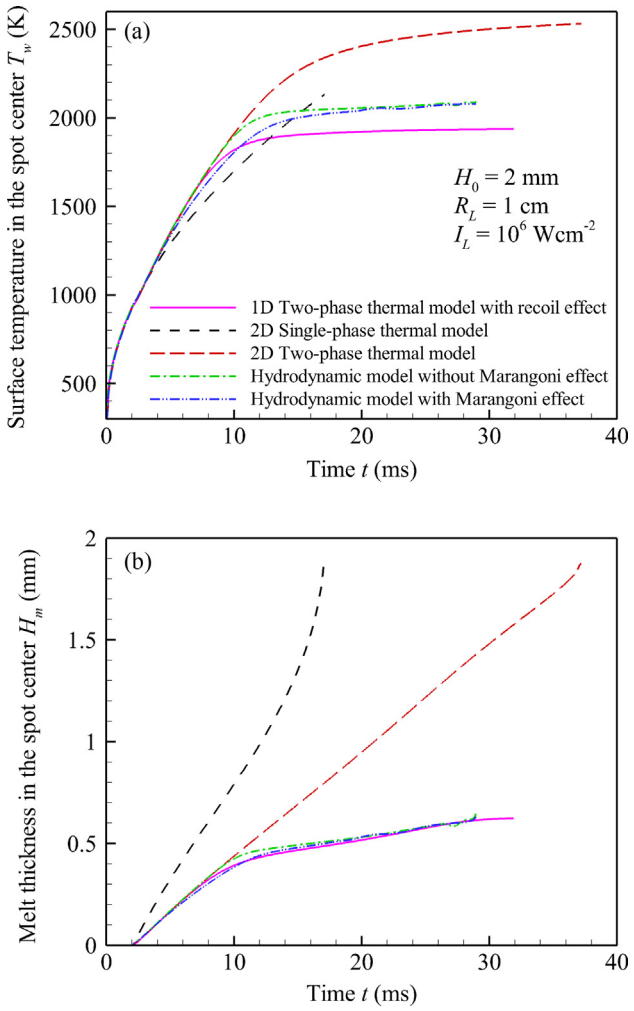

Fig. 9. Surface temperature T_w (a) and thickness of the molten layer H_m (b) in the spot center versus time t obtained in simulations of CW melting of an aluminum film with thickness $H_0 = 2$ mm, FWHM spot radius $R_L = 1$ cm, and laser intensity $I_L = 10^6$ W cm^{-2}. Solid curve: 1D two-phase thermal model with the melt expulsion described by Eq. (17c); short-dash curve: 2D one-phase thermal model, Eq. (14), where $h = C_S T$; long-dash curve: 2D two-phase thermal model; dash-dotted curve: Hydrodynamic model with the recoil pressure effect, but without the Marangoni effect; dash-double-dotted curve: Hydrodynamic model with both the recoil pressure and Marangoni effects. The values of H_m for the short-dash curve in panel (b) correspond to the position of the isotherm $T = T_m$. The right-most point of each curve corresponds to the melt-through time t_m.

irregular complex shape of the free surface in the vicinity of the edge (Fig. 11(d, e)). At smaller I_L, similar waves are formed, but their wavelengths, which are determined by the gradient of the surface temperature, remain larger or comparable to the radial size of the molten pool.

Our numerical approach is not well suited for simulations where irregular free surfaces and strong variations of the height function $H_m(r, t)$, characteristic for the single-wave regime illustrated in Fig. 11, appear. The strong distortions of the computational mesh introduce large errors in the mass conservation, the condition of the divergence-free velocity filed is difficult to satisfy, and the iterative scheme used for solving the non-linear finite-difference equations starts to diverge. These technical difficulties prevent us from extending the simulations where pronounced surface waves are generated up to the time of full melting of the film at the center of the laser spot. The melt-through time shown in Fig. 12, therefore, was determined only in a limited range of I_L, where accurate solution of the hydrodynamic equations was possible up to the time $t = t_m$.

Fig. 12(a) illustrates the overall contribution of the Marangoni and recoil pressure effects to the melt-through time t_m. Two families of points are obtained with the hydrodynamic model, where the Marangoni effect is either included or not accounted for. These results clearly show that the Marangoni effect results in only marginal additional decrease of t_m in a narrow range of I_L, from $\sim 10^5$ W cm^{-2} to $\sim 6 \times 10^5$ W cm^{-2}. The negligible effect of Marangoni stresses at smaller I_L is explained by relatively small surface gradients of temperature and small magnitude of $\tau_{w\tau}$. The small overall effect of Marangoni stresses at larger I_L is observed due to the fast decrease in t_m, so that even strong tangential stresses cannot substantially change the total radial momentum of the fluid since the time they act on the fluid is too short.

Fig. 12(b) demonstrates the overall contribution of the recoil effect to the melt-through time. All points are obtained without the Marangoni stresses. At the lower end of the considered range of I_L, the data points obtained with the hydrodynamic model practically coincide with the points obtained with the 2D thermal model, where the melt expulsion is not accounted for. This means that melting of the film does not depend on fluid flow and is fully controlled by the Stefan condition on the melting front. At the same time, the values of t_m predicted with the hydrodynamic and 2D thermal models are larger than values obtained with the 1D model. This observation demonstrates that thermal transport in the radial direction is important here, since the melt-through time is relatively long. With increasing I_L, the results of hydrodynamic simulations deviate from the data point predicted with the

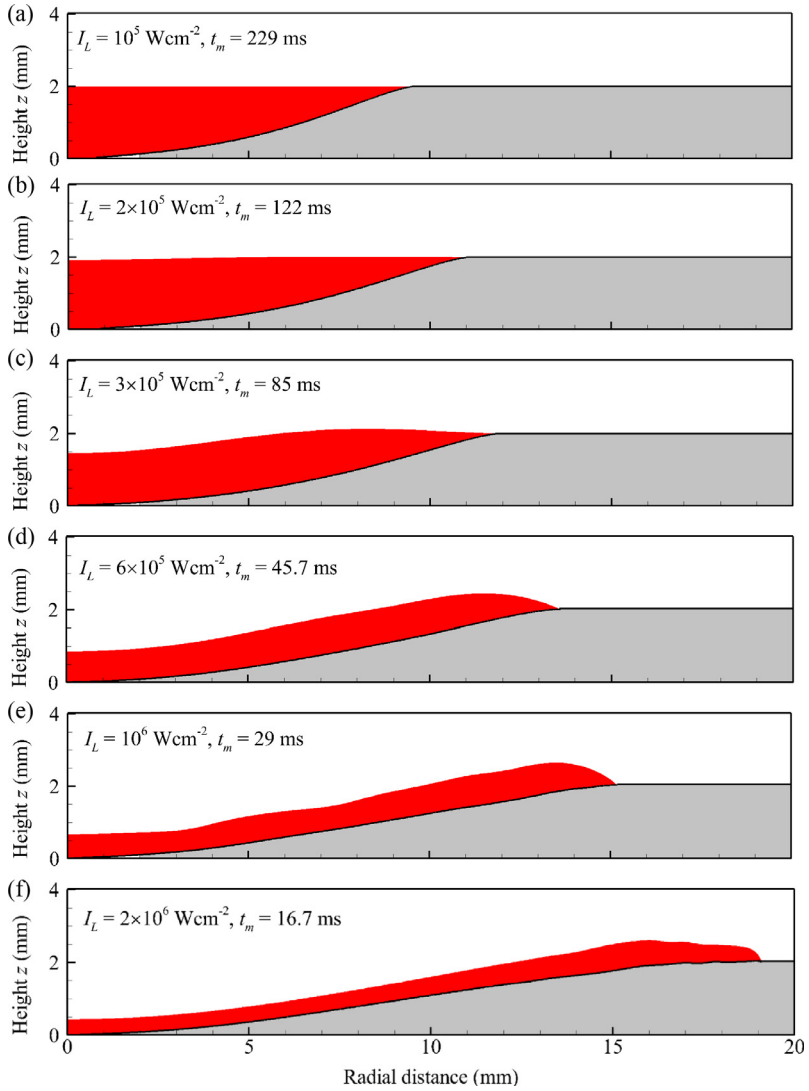

Fig. 10. The shape of the molten pool (red region) at $t = t_m$ predicted in simulations of laser melting of an aluminum film with thickness $H_0 = 2$ mm, FWHM laser spot radius $R_L = 1$ cm, and laser intensity $I_L = 10^5$ W cm^{-2} (a), 2×10^5 W cm^{-2} (b), 3×10^5 W cm^{-2} (c), 6×10^5 W cm^{-2} (d), 10^6 W cm^{-2} (e), and 2×10^6 W cm^{-2} (e). The recoil effect from the evaporation is accounted for in the simulations, while the Marangoni effect is not taken into account. The melt-though time t_m for each simulation is shown in the figure panels. (For interpretation of the references to color in this figure legend, the reader is referred to the web version of this article.)

2D thermal model and approach the points obtained with the 1D thermal model of melting, where melt expulsion is accounted for with Eq. (17c). This indicates that the effect of heat transfer in the radial direction tends to be less important with decreasing t_m, but the effect of melt expulsion becomes more significant. Close to the upper boundary of the considered range of I_L the melt-through time predicted with the hydrodynamic model is somewhat smaller than t_m calculated based on the 1D thermal model. Nevertheless the simple 1D model provides a decent agreement in the melt-through time with the much more sophisticated hydrodynamic model. It is worth noting that one can formally obtain a perfect agreement between the 1D thermal and 2D hydrodynamic model at large I_L by adjusting the slab radius R_L in Eq. (17c), which is a free parameter of the 1D thermal model and does not have to be precisely equal to the FWHM radius of the laser spot, as it was assumed in calculations presented in Fig. 12.

5.2. Effect of the film thickness

The investigation of melt flow for different film thicknesses shows that the critical laser intensity required for the onset of significant melt expulsion is not a universal parameter, but has a strong dependence on H_0. This conclusion is illustrated by Figs. 13 and 14. In particular, the shape of the molten pool at a time slightly smaller than t_m obtained for a film of thickness $H_0 = 4$ mm at $I_L = 2 \times 10^5$ W cm^{-2} is shown in Fig. 13. At this laser intensity, material removal by evaporation is negligible and the decrease in the thickness of the molten layer at the spot center is caused only by melt expulsion induced by the recoil pressure effect. This result is drastically different from the one shown for the same I_L but for the twice thinner film in Fig. 10(b), where the effect of melt redistribution is barely noticeable.

The comparison of results obtained with and without the recoil effect indicates the crucial role of the delay time τ_d for the development of melt flow under the recoil pressure effect in films with different thickness (Fig. 14). For the film with $H_0 = 2$ mm, the melt-through time t_m at $I_L = 2 \times 10^5$ W cm^{-2} is practically equal to the expulsion waiting time and, therefore, is too short to allow for the development of any significant melt flow. An increase in the film thickness at a fixed I_L retains almost the same surface temperature in the center of the laser spot at the onset of expulsion, $T_w \approx 1600$ K, and only slightly increases τ_d (with increasing H_0

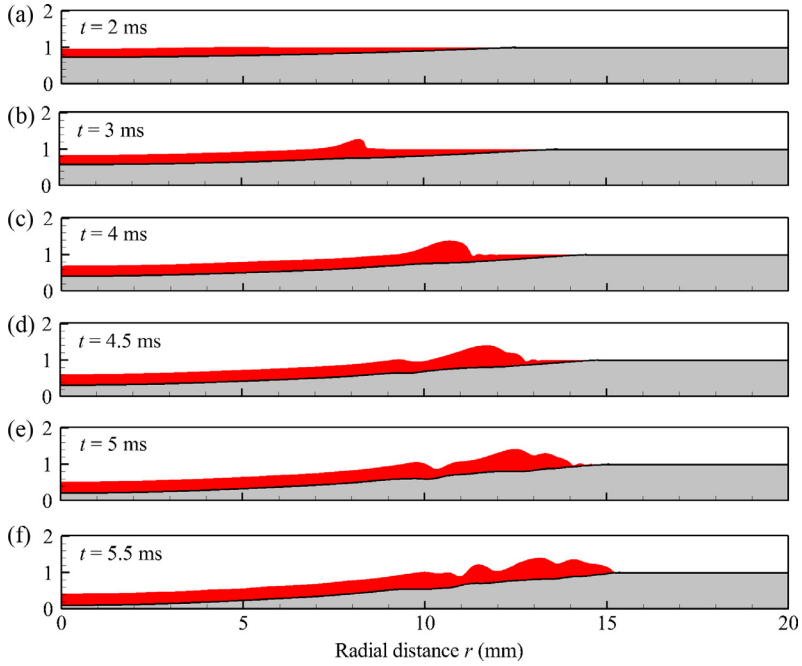

Fig. 11. The evolution of the shape of the molten pool (red region) during laser melting of an aluminum film of thickness $H_0 = 1$ mm with a CW laser of intensity $I_L = 3 \times 10^6$ W cm^{-2} and FWHM laser spot radius $R_L = 1$ cm. The snapshots from the simulation are taken at times t of 2 ms (a), 3 ms (b), 4 ms (c), 4.5 ms (d), 5 ms (e), and 5.5 ms (f). The recoil effect from the evaporation is accounted for in the simulation, while the Marangoni effect is not taken into account. (For interpretation of the references to color in this figure legend, the reader is referred to the web version of this article.)

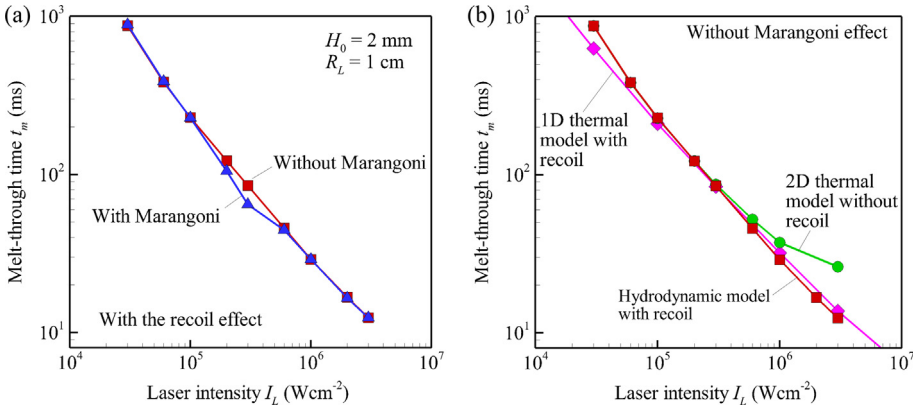

Fig. 12. Melt-through time t_m versus laser intensity I_L obtained for an aluminum film with thickness $H_0 = 2$ mm and FWHM spot radius $R_L = 1$ cm. All points shown in panel (a) are obtained with the hydrodynamic model with the recoil effect and with (triangles) or without (squares) the Marangoni effect accounted for. All points shown in panel (b) are obtained without the Marangoni effect with the 2D thermal model (circles), hydrodynamic model with the recoil effect (squares), and 1D thermal model where the melt expulsion is described by Eq. (17c) (diamonds). Squares in both panels represent the results of the same simulations. In panel (b), circle and square symbols visually coincide with each other at small intensities, $I_L \leqslant 2 \times 10^5$ W cm^{-2}. All symbols show the results of the simulations, while curves are guides to the eye.

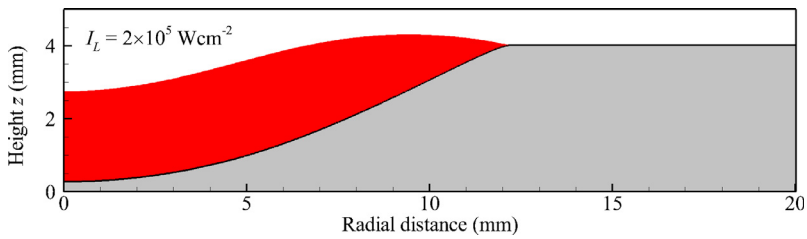

Fig. 13. The shape of the molten pool (red region) at $t = 279$ ms obtained in a simulation of laser melting of an aluminum film with thickness $H_0 = 4$ mm, FWHM laser spot radius $R_L = 1$ cm, and laser intensity $I_L = 2 \times 10^5$ W cm^{-2}. The recoil effect from evaporation is accounted for, while the Marangoni effect is not taken into account. (For interpretation of the references to color in this figure legend, the reader is referred to the web version of this article.)

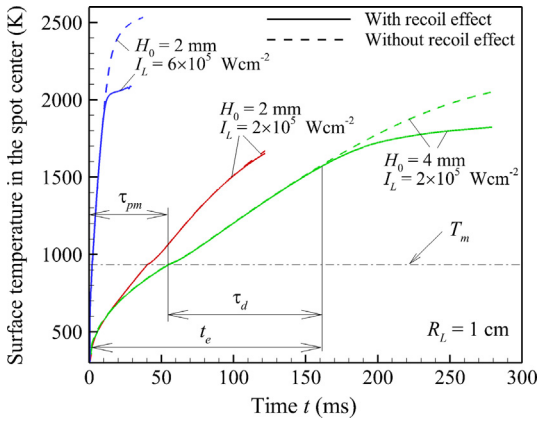

Fig. 14. Surface temperature in the laser spot center T_w versus time t obtained in hydrodynamic simulations performed with (solid curves) and without (dashed curves) the recoil pressure effect. All simulations are performed without the Marangoni effect and for the laser spot radius $R_L = 1$ cm. The film thickness H_0 and laser intensity I_L are shown for each simulation in the figure panel. The dash-dotted line corresponds to the melting temperature T_m. The times of the onsets of melting, τ_{pm}, and melt expulsion, $t_e = \tau_{pm} + \tau_d$ are shown for the simulation performed with $H_0 = 4$ mm and $I_L = 2\times\ 10^5$ W cm^{-2}. The right-most point of each curve corresponds to the melt-through time t_m.

melting of a film eventually starts to resemble melting of a bulk target). The melt-through time for the thicker film, however, is longer than the expulsion waiting time, so that pronounced melt expulsion due to the recoil pressure effect can be seen in Fig. 13. At a fixed $H_0 = 2$ mm, an increase in I_L results in the strong decrease of both τ_d and t_m, but the delay time decreases faster, so that eventually the recoil pressure effect becomes important as can be seen from the comparison between pairs of blue ($I_L = 6 \times 10^5$ W cm^{-2}) and red[1] ($I_L = 2 \times 10^5$ W cm^{-2}) curves in Fig. 14. Thus, the existence of the delay time for the onset of melt expulsion introduces the factor of time into the phenomenon of laser melting of thin films and makes the threshold laser intensity for the onset of melt expulsion dependent on the film thickness.

5.3. Small laser spot size

The decrease in the laser spot radius should increase the gradient of surface temperature in the radial direction and, consequently, the magnitude of the Marangoni stresses. Therefore, it is natural to expect that focusing of the laser beam on a smaller spot on the target might significantly enhance the effect of the Marangoni stresses on the shape of the molten pool and melt-through time. The simulations, however, clearly show that this is not the case, and the Marangoni stresses have little effect on the overall process of melt flow and the melt-through time even when the laser spot size is decreased by two orders of magnitude with respect to the spots considered in the previous sections. This is illustrated below by the results of simulations performed for the laser spot radius $R_L = 0.1$ mm, film thickness $H_0 = 0.2$ mm, and a range of laser intensities I_L from 2×10^6 W cm^{-2} to 2×10^8 W cm^{-2} (Figs. 15–17). The simulations are performed with the time step $\Delta t = 0.1$ μs and dimensions of the computational domain $L_0 = 0.4$ mm and $L_1 = 1.6$ mm (see Fig. 1).

The temperature and radial velocity fields are shown for a simulation performed with $I_L = 3 \times 10^7$ W cm^{-2} in Fig. 15. Similar to the results obtained for a much larger spot and discussed above, the thickness of the molten pool and the melt-through time predicted with the two-phase 2D thermal model without fluid flow (Fig. 15(a)) exhibit large deviations from the results of hydrodynamic simulations. The change in the shape of the free surface is caused here solely by evaporation, which is more intense than in the case of large spot due to an order of magnitude decrease in H_0 and an increase in the laser intensity leading to higher surface temperatures and vapor fluxes. The recoil pressure effect decreases the surface temperature in the center of the laser spot at $t = t_m$ by ~17% and reduces the thickness of the molten layer by more than a factor of two (Fig. 16).

The hydrodynamic simulations performed without (Fig. 15(b, d)) and with (Fig. 15(c, e)) the Marangoni effect predict almost identical terminal temperature fields, shapes of the surface of the molten pool, and melt-through times. At the same time, the field of the radial velocity is strongly affected by the Marangoni stresses that induce two orders of magnitude increase in the maximum value of u. This strong radial velocity appears, however, only in a very thin layer of the melt near the free surface. The hydrodynamic simulations with I_L above a certain level predict the development of quasi-periodic oscillations of the whole molten layer that shows up as the oscillating surface temperature and thickness of the molten layer in Fig. 16. These oscillations appear even in the case when flow of the molten material is driven by only the recoil pressure effect, but the magnitude of the oscillations is greatly enhanced by the Marangoni stresses. Due to stronger deformation of the computational mesh, the numerical errors in the simulations of small laser spots are larger than in the simulations performed for larger spot sizes and comparable laser intensities. Thus, further investigations are required in order to establish whether these oscillations are numerical artifacts or evolve due to an intrinsic instability of the melt flow.

The relationships between the results obtained with different models and shown in Fig. 16 look similar to those shown in Fig. 9 for the larger spot. It is remarkable that, in both cases, the predictions of the simple 1D thermal model, where melt expulsion is accounted for with Eq. (17c), are in an excellent agreement with results of full hydrodynamic simulations in terms of the thickness of the molten layer and in an acceptable agreement in terms of the surface temperature at the spot center. At the same time, under conditions illustrated in Fig. 16, the 1D model underestimates the melt-through time by about a factor of two. As can be seen from the result shown in Fig. 17, this happens because at $I_L = 3 \times 10^7$ W cm^{-2} the effect of heat transfer in the radial direction is still strong for small R_L and cannot be neglected. At higher I_L, when the effect of radial thermal transport gradually diminishes, the melt-through time calculated with the 1D model gets into a good agreement with the results of hydrodynamic simulations.

The small effect of the Marangoni stresses on the melt-through time is explained by the fact that the melt-though time decreases roughly by two orders of magnitude with respect to the case of the larger spot size, i.e. roughly proportionally to the variation of the spot size itself (Fig. 17). Under these conditions, the strong Marangoni stresses are able to induce large radial velocity only in a thin layer close to the free surface of the molten pool, but contribution of this layer to the overall flow of the melt in the radial direction remains small.

The comparison of the melt-through time obtained for the small spot size with the 2D thermal and hydrodynamic models and with 1D thermal model, where the recoil effect is accounted for with Eq. (17c), reveals the same three regimes of melting that were previously established for larger laser spots (see Figs. 12(b) and 17). At small laser intensities, $I_L \leqslant 8 \times 10^7$ W cm^{-2}, the meting process is dominated by heat transfer in the radial direction and the recoil effect is negligible, so that the 2D thermal and hydrodynamic models predict almost identical t_m. At large laser intensities,

[1] For interpretation of color in Fig. 14, the reader is referred to the web version of this article.

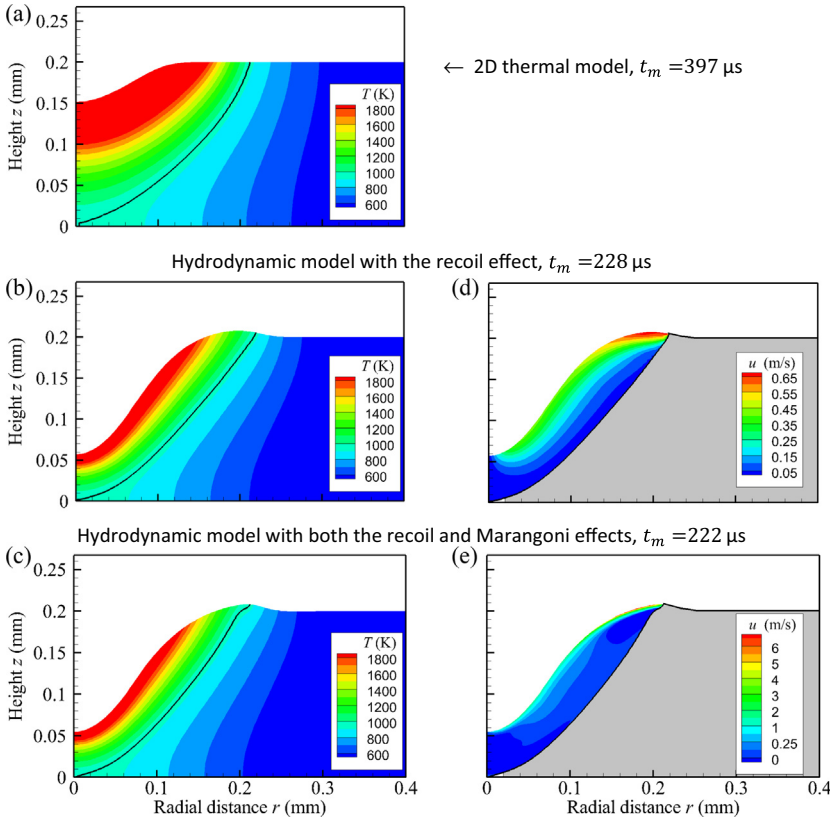

Fig. 15. Temperature T (a-c) and radial velocity u (d, e) fields obtained by the time $t = t_m$ with the 2D thermal model without fluid flow (a), and hydrodynamic model with the recoil effect (b, d), and with both the recoil and Marangoni effects (c, e) for the film thickness $H_0 = 0.2$ mm, FWHM spot radius $R_L = 0.1$ mm, and laser intensity $I_L = 3 \times 10^7$ W cm^{-2}. The melt-through time t_m is indicated in the figure panels. The black curves mark the positions of solid-liquid interfaces where $T = T_m$ and the gray areas in panels (d, e) correspond to the solid material.

$I_L \gtrsim 8 \times 10^7$ W cm^{-2}, the heat transfer in the radial direction is irrelevant for the melt-through time, the thickness of the molten layer at the spot center becomes small as compared to the film thickness, and the results of hydrodynamic simulations approach the predictions obtained with the 1D thermal model. With further increase in laser intensity the overall significance of the recoil effect gradually decreases due to the decrease in the thickness of the molten layer. The transition between these two regimes occurs as I_L varies within about one order of magnitude. This picture of transition from the radial heat transfer-dominated to the expul sion/evaporation-dominated regimes is more pronounced here than in the case of the larger spot in Fig. 12(b), since the effect of heat transfer in the radial direction becomes more important for smaller spot sizes. It is worth noting that the close agreement between the melt-through times obtained with the hydrodynamic and 1D thermal models at $I_L = 10^8$ W cm^{-2} does not imply that these models will produced identical t_m at larger laser intensities. Similar to the case of the larger spot, we believe that the 1D thermal model will slightly overestimate the melt-through time at $I_L > 10^8$ W cm^{-2}. At these large intensities, however, our numerical approach for hydrodynamic simulations predicts unstable melt flows and does not allow us to accurately determine the melt-through times.

6. Conclusions

Direct hydrodynamic simulations of CW laser melting of thin aluminum films with thickness smaller or equal than the laser spot diameter reveal only a marginal effect of the Marangoni stresses on the overall picture of melt flow and the melt-through time. This result is explained by the relatively short time required for melting of the film to its full depth and a small viscosity of liquid aluminum, so that the Marangoni stresses are not capable of inducing strong radial flow velocities through the whole depth of the molten pool.

The direct hydrodynamic simulations as well as analysis based on a simple 1D thermal model, where the expulsion velocity is accounted for based on the Bernoulli integral, demonstrate that the efficiency of melt expulsion is not defined by the surface temperature alone, but is constrained by the characteristic thickness of the molted layer. The recoil effect is capable of strongly decreasing the melt-through time in a certain range of laser intensity. At laser intensities below this range, the melt-through time is relatively long and the melting is dominated by heat transfer in the radial direction, while the vapor pressure is too low to produce a substantial melt expulsion velocity. At laser intensities above this range, the melt-through time is relatively short, the molten layer is shallow, and the efficiency of melt expulsion becomes low, so that the melt-through time is largely controlled by evaporation from the molten pool.

The range of laser intensities where the melt-through time is dominated by the recoil pressure effect is not unique but is strongly affected by the film thickness. The film thickness dependence is explained by the existence of a time delay between the onset of melting and the onset of melt expulsion. During this time delay, the thickness of the molten pool increases up to a level where melt expulsion starts to strongly affect the motion of the solid-liquid interface. For a fixed laser intensity, the melt expulsion plays a minor role in the damage of thin films, when the

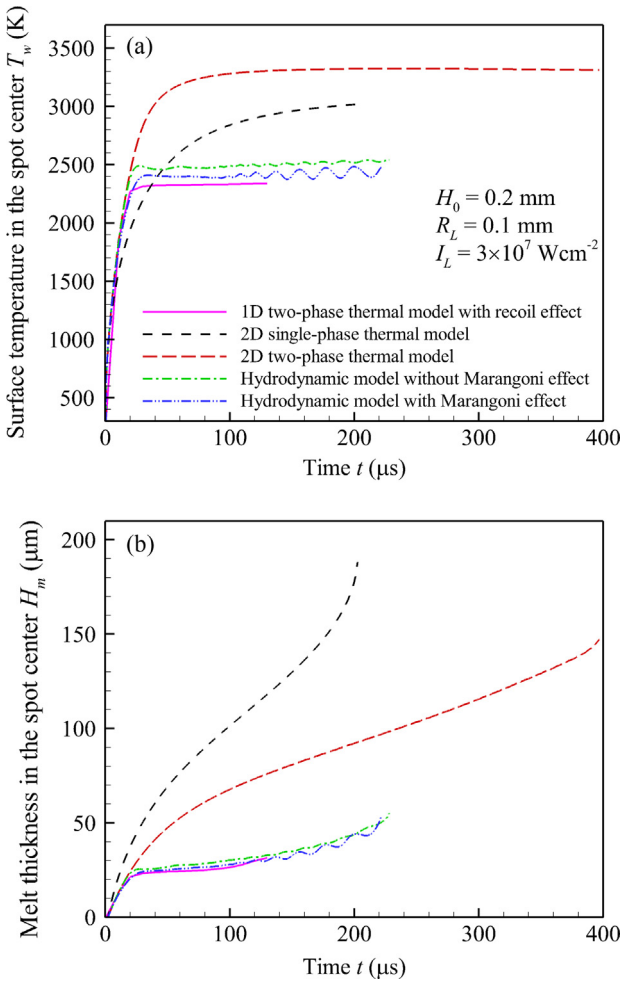

Fig. 16. Surface temperature T_w (a) and thickness of the molten layer H_m (b) in the spot center versus time t obtained in simulations of CW melting of an aluminum film with thickness $H_0 = 0.2$ mm, FWHM spot radius $R_L = 0.1$ mm, and laser intensity $I_L = 3 \times 10^7$ W cm^{-2}. Solid curve: 1D two-phase thermal model with the melt expulsion described by Eq. (17c); short-dash curve: 2D one-phase thermal model with Eq. (14), where $h = C_S T$; long-dash curve: 2D two-phase thermal model; dash-dotted curve: Hydrodynamic model with the recoil effect, but without the Marangoni effect; dash-double-dotted curve: Hydrodynamic model with both the recoil and Marangoni effects. Values of H_m for the short-dash curve in panel (b) are determined from the position of the isotherm $T = T_m$. The right-most point of each curve corresponds to the melt-through time t_m.

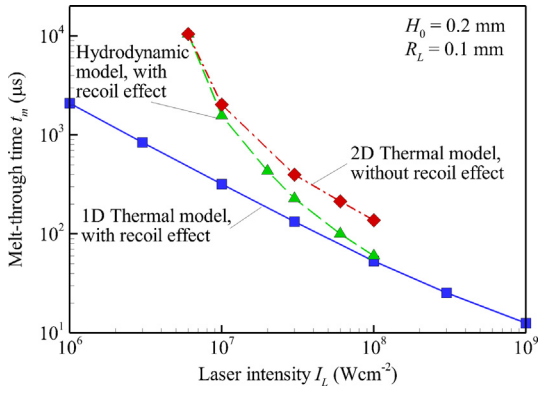

Fig. 17. Melt-through time t_m versus laser intensity I_L obtained for the film thickness $H_0 = 0.2$ mm and FWHM spot radius $R_L = 0.1$ mm with the 1D thermal model, where the melt expulsion is described by Eq. (17c) (square symbols), 2D thermal model without the recoil effect (diamond symbols), and hydrodynamic model with the recoil effect (triangle symbols). In hydrodynamic simulations, the Marangoni effect is not accounted for. All symbols show the results of the simulations, while curves are guides to the eye.

melt-through time is smaller than the waiting time for the onset of melt expulsion. On the contrary, the recoil effect can be prominent for thicker films, when the melt-through time is longer than the expulsion waiting time.

A simple two-phase 1D thermal model of CW laser melting, where the expulsion velocity is accounted for based on the Bernoulli integral, is developed and found to be capable of accurate prediction of the melt-through time above a certain level of laser intensity. This model also captures qualitative trends in the variation of the process parameters even for lower laser intensities and is recommended as a robust engineering tool for the first-order evaluation of the CW laser damage of metal films.

Acknowledgements

Financial support for this work is provided by the Air Force Office of Scientific Research (Grant FA9550-10-1-0541). A.V. also acknowledges support through the NSF CAREER award CMMI-1554589. Computational support is provided by the Alabama Supercomputer Center and NSF XSEDE (project TG-DMR130010).

References

[1] J. Dowden (Ed.), The Theory of Laser Materials Processing. Heat and Mass Transfer in Modern Technology, Springer Series in Materials Science, vol. 119, Springer, Dordrecht, The Netherlands, 2009.
[2] C.D. Boley, K.P. Cutter, S.N. Fochs, P.H. Pax, M.D. Rotter, A.M. Rubenchik, Interaction of a high-power laser beam with metal sheets, J. Appl. Phys. 107 (2010) 043106.
[3] W.-K. Baek, K.-C. Lee, S.-I. An, W.-S. Shin, J.J. Yoh, Melt-through characteristics in continuous beam irradiation of flying metal samples in flow speeds up to 85 m/s, Opt. Laser Technol. 45 (2013) 250–255.
[4] C. Earl, J.R. Castrejón-Pita, P.A. Hilton, W. O'Neill, The dynamics of laser surface modification, J. Manuf. Proc. 21 (2016) 214–223.
[5] S.M. Baumann, B.E. Hurst, M.A. Marciniak, G.P. Perram, Fiber laser heating and penetration of aluminum in shear flow, Opt. Eng. 53 (2014) 122510.
[6] W.R. Harp, J.R. Dilwith, J.F. Tu, Laser ablation using a long-pulsed, high-fluence, CW single-mode fiber laser, J. Mater. Process. Tech. 198 (2008) 22–30.
[7] D. Bäuerle, Laser Processing and Chemistry, Springer, Berlin, 2000.
[8] A. Miotello, R. Kelly, Critical assessment of thermal models for laser sputtering at high fluences, Appl. Phys. Lett. 67 (1995) 3535–3537.
[9] N.M. Bulgakova, A.V. Bulgakov, Pulsed laser ablation of solids: transition from normal vaporization to phase explosion, Appl. Phys. A 73 (2001) 199–208.
[10] L.V. Zhigilei, Z. Lin, D.S. Ivanov, Atomistic modeling of short pulse laser ablation of metals: connections between melting, spallation, and phase explosion, J. Phys. Chem. C 113 (2009) 11892–11906.
[11] A.N. Volkov, L.V. Zhigilei, Computational study of the role of gas-phase oxidation in CW laser ablation of Al target in an external supersonic air flow, Appl. Phys. A 110 (2013) 537–546.
[12] K. Chen, Y.L. Yao, V. Modi, Numerical simulation of oxidation effects in the laser cutting process, Int. J. Adv. Manuf. Technol. 15 (1999) 835–842.
[13] V. Semak, A. Matsunawa, The role of recoil pressure in energy balance during laser materials processing, J. Phys. D: Appl. Phys. 30 (1997) 2541–2552.
[14] B.S. Yilbas, S.B. Mansoor, Laser evaporative heating of surface: simulation of flow field in the laser produced cavity, J. Phys. D: Appl. Phys. 39 (2006) 3863–3875.
[15] S.P. Harimkar, A.N. Samant, N.B. Dahotre, Temporally evolved recoil pressure driven melt infiltration during laser surface modifications of porous alumina ceramic, J. Appl. Phys. 101 (2007) 054911.
[16] S.A. Khairallah, A. Anderson, Mesoscopic simulation model of selective laser melting of stainless steel powder, J. Mater. Proc. Technol. 214 (2014) 2627–2636.
[17] Y.L. Yao, H. Chen, W. Zhang, Time scale effects in laser material removal: a review, Int. J. Adv. Manuf. Technol. 26 (2005) 598–608.
[18] V. Sarou-Kanian, F. Millot, J.C. Rifflet, Surface tension and density of oxygen-free liquid aluminum at high temperature, Int. J. Thermophys. 24 (2003) 277–286.
[19] V.S. Ajaev, D.A. Willis, Thermocapillary flow and rupture in films of molten metal on a substrate, Phys. Fluids 15 (2003) 3144–3150.
[20] D.A. Willis, X. Xu, Transport phenomena and droplet formation during pulsed laser interaction with thin films, J. Heat Transfer 122 (2003) 763–769.
[21] K.C.A. Crane, R.K. Garnsworthy, L.E.S. Mathias, Ablation of materials subjected to laser radiation and high-speed gas flows, J. Appl. Phys. 51 (1980) 5954–5961.
[22] D. Schuöcker, Dynamic phenomena in laser cutting and cut quality, Appl. Phys. B 40 (1986) 9–14.
[23] G.V. Ermolaev, O.B. Kovalev, Simulation of surface profile formation in oxygen laser cutting of mild steel due to combustion cycles, J. Phys. D: Appl. Phys. 42 (2009) 185506.

[24] Y. Zhang, Z. Shen, X. Ni, Modeling and simulation on long pulse laser drilling processing, Int. J. Heat Mass Transfer 73 (2014) 429–437.
[25] A. Ben-Yakar, A. Harkin, J. Ashmore, R.L. Byer, H.A. Stone, Thermal and fluid processes of a thin melt zone during femtosecond laser ablation of glass: the formation of rims by single laser pulses, J. Phys. D: Appl. Phys. 40 (2007) 1447–1459.
[26] L. Han, F.W. Liou, Numerical investigation of the influence of laser beam model on melt pool, Int. J. Heat Mass Transfer 47 (2004) 4385–4402.
[27] W.D. Bennon, F.P. Incopera, A continuum model for momentum, heat, and species transport in binary solid-liquid phase change systems – I. Model formulation, Int. J. Heat Mass Transfer 30 (1987) 2161–2170.
[28] C. Cercignani, Rarefied Gas Dynamics: From Basic Concepts to Actual Calculations, Cambridge University Press, Cambridge, 2000.
[29] S.B.G. O'Brien, L.W. Schwartz, Theory and modeling of thin film flows, in: Encyclopedia of Surface and Colloid Science, Marcel Dekker, New York, 2002, pp. 5283–5297.
[30] R.H. Pletcher, J.C. Tannehill, D. Anderson, Computational Fluid Mechanics and Heat Transfer, third ed., CRC Press, New York, 2012.
[31] S.E. Rogers, D. Kwak, Upwind differencing Scheme for the time-accurate incompressible Navier-Stokes equations, AIAA J. 28 (1990) 253–262.
[32] S.E. Rogers, D. Kwak, An upwind differencing scheme for the incompressible Navier-Stokes equations, Appl. Numer. Math. 8 (1991) 43–64.
[33] U. Chia, K.N. Chia, C.T. Shin, High-Re solutions for incompressible flow using the Navier-Stokes equations and a multigrid method, J. Comput. Phys. 48 (1982) 387–411.
[34] E. Erturk, Discussions on driven cavity flow, Int. J. Numer. Meth. Fluids 60 (2009) 275–294.
[35] P.D. Thomas, C.K. Lombard, Geometric conservation law and its application to flow computations on moving grids, AIAA J. 17 (1979) 1030–1037.
[36] H. Schlichting, K. Gersten, Boundary-Layer Theory, eighth ed., Springer-Verlag, New York, 2000.
[37] C.K. Chun, S.O. Park, A fixed-grid finite-difference method for phase-change problems, Numer. Heat Transfer B 38 (2000) 59–73.
[38] http://volkov.end.ua.edu.
[39] M.J. Assael, K. Kakosimos, R.M. Banish, J. Brillo, I. Egry, R. Brooks, P.N. Quested, K.C. Mills, A. Nagashima, Y. Sato, W.A. Wakeham, Reference data for the density and viscosity of liquid aluminum and liquid iron, J. Phys. Chem. Ref. Data 35 (2006) 285–300.
[40] Z.H. Shen, S.Y. Zhang, J. Lu, X.W. Ni, Mathematical modeling of laser induced heating and melting in solids, Opt. Laser Technol. 33 (2001) 533–537.